Design and Adaptation of a Folded Split Ring Resonator Antenna for an Animal Borne Sensor

by

Samuel Christopher Keightley Dodson

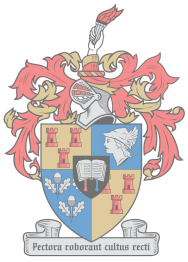

Thesis presented in partial fulfilment of the requirements for the degree of Master of Electrical and Electronic Engineering in the Faculty of Engineering at Stellenbosch University

Supervisor: Dr. P.G. Wiid

Co-supervisor: Professor T.R. Niesler

March 2018

The author gratefully acknowledges support by the National Research Foundation, by Telkom South Africa, and by Innovus of Stellenbosch University.

Declaration

By submitting this thesis electronically, I declare that the entirety of the work contained therein is my own, original work, that I am the sole author thereof (save to the extent explicitly otherwise stated), that reproduction and publication thereof by Stellenbosch University will not infringe any third party rights and that I have not previously in its entirety or in part submitted it for obtaining any qualification.

Date: March 2018

Abstract

This thesis describes the selection, design, adaptation and construction of a folded split ring resonator (FSRR) antenna to replace the existing transmitting antenna in an animal-borne behavioural monitoring system (ABBMS). The antenna is required to fit completely inside a small rectangular enclosure of dimension $105 \times 65 \times 26\ mm$, which is attached to the rear leg of a rhinoceros. An FSRR antenna is selected from a group of candidate antennas based on its high radiation and reflection efficiencies e_{rad} and e_{ref}, quasi-isotropic radiation pattern, small electrical size and availability of impedance tuning mechanisms. A prototype model is designed and optimised in FEKO simulation software and is manufactured on FR-4 substrate. It is then compared to a similar FSRR design from the literature and is found to behave similarly, even though the substrate on which our prototype is constructed is more affordable. The prototype is then adapted to fit inside the enclosure. The prototype antenna is reduced from a 3-dimensional to a planar form to incorporate a small surface mount balun. The planar model is transformed from a circular shape to a rectangular shape, and a thicker FR-4 substrate is included. The length and breadth of the antenna are set to 103.5 mm and 63.5 mm respectively. These transformations reduce the e_{ref} and e_{rad} values. However, the model now fits inside the enclosure. The feed of the rectangular model is subsequently inverted to face inward, to allow the incorporation of sensor electronics onto the antenna's substrate in the future. This further decreases e_{ref}. The e_{ref} is increased by adjusting the inner-feed antenna's tuning parameters. The resulting model is constructed and compared to the first circular prototype. It is shown to operate with higher e_{ref} and it also maintains the quasi-isotropic radiation pattern. However, the thick FR-4 substrate decreases the e_{rad}. This decreases the realised gain below the requirement. It is recommended to use a low loss substrate, of a similar permittivity, to alleviate this.

Uittreksel

Hierdie proefskrif beskryf die keuse, ontwerp, aanpassing en konstruksie van 'n gevoude verdeelring resonator (FSRR) antenna om die bestaande transmissie antenna in 'n dier-gemonteerde gedragsmoniteringstelsel (ABBMS) te vervang. Die antenna word benodig om binne 'n klein reghoekige omhulsel van afmetings $105 \times 65 \times 26$ mm te pas, wat aan die agterbeen van 'n renoster gekoppel is. 'n Sirkelvormige FSRR-antenna word gekies uit 'n lys kandidaat-antennas, gebaseer op sy hoë stralings en weerkaats-doeltreffendheid e_{rad} en e_{ref}, kwasi-isotropiese stralingspatroon, klein elektriese grootte en beskikbaarheid van impedansie-aanpassingsmeganismes. 'n Optimale prototipe model is ontwerp in FEKO simulasie sagteware en is vervaardig met FR-4 substraat. Dit vergelyk goed met 'n soortgelyke FSRR-ontwerp, selfs al is die substraat waarop ons prototipe gebou is, meer bekostigbaar. Die prototipe word dan aangepas om binne die omhulsel te pas. Die 3-dimensionele prototipe antenna word verminder tot 'n planêre vorm sodat 'n klein oppervlak-gemonteerde balun daarop ingewerk kan word. Die prototipe word omskep van 'n sirkelvorm na 'n reghoekige vorm wat 'n dikker FR-4-substraat bevat. Die lengte en breedte van die antenna word onderskeidelik gestel op 103.5 mm en 63.5 mm. Die transformasies verminder die e_{ref} en e_{rad} van die antenna. Die model pas egter nou in die omhulsel. Die voer van hierdie model word dan omgekeer om na binne te wys, sodat sensorelektronika in die toekoms op die antenna se substraat geïntegreer kan word. Dit verminder verder e_{ref}. Die e_{ref} word verhaal deur toepaslike verandering aan die reghoekige antenna se aanpassingsparameters. Die gevolglike model is vervaardig en vergelyk met die eerste prototipe en toon 'n hoër e_{ref}. Dit handhaaf ook die kwasi-isotropiese stralingspatroon. Die dikker substraat waarop dit gedruk is, verminder egter die e_{rad}. Dit verminder die gerealiseerde aanwinste benede die vereistes. Dit word aanbeveel om 'n lae-verlies substraat, van 'n soortgelyke permittiwiteit, te gebruik om

dit te verlig.

Acknowledgements

Firstly, I would like to express my gratitude to Dr. Gideon Wiid, my supervisor. Your time and dedication given towards helping me complete this thesis were invaluable. To my co-supervisor, Professor Thomas Niesler, thank you for organising this wonderful project, providing me with encouragement and doing an excellent job at correcting my writing.

Thank you to Wessel Croukamp and Wynand van Eeden for helping me turn my antenna simulations into the real deal. To Wessel: I will miss our chats about your home projects and my surfing exploits.

I really enjoyed the company of my fellow E207 office members; Nancy Omollo, Stanley Kuja, Christopher Atkinson (when he was there), as well as the lunch-time visits from Temwani Phiri. The few outings that we had together were always memorable, and maybe I can take all of you (including Chris and TJ) to Fish Hoek one of these days.

My family have been incredibly supportive throughout my University career. You are all so patient and willing to listen to any and all of my concerns. To my Mom and Dad, I've been very lucky to have you guys come down relatively frequently. To my brothers, I miss you both and really appreciate any time we do spend together. Thanks to my girlfriend, Laura for also staying supportive through a very busy 2017. I know you have your own things to worry about, yet you still somehow have the energy to take care of me!

Contents

List of Figures

List of Tables

Nomenclature

Variables

ka	Relative Size	[Dimensionless]
Q	Quality Factor	[Dimensionless]
D	Directivity	[dBi]
G	Gain	[dBi]
G_{rl}	Realised Gain	[dBi]
Γ	Reflection Coefficient	[dB]
e_{ref}	Reflection Efficiency	[%]
e_{rad}	Radiation Efficiency	[%]
e_{tot}	Total Efficiency	[%]

Acronyms

ABBMS Animal Borne Behavioural Monitoring System

AUT Antenna Under Test

ESA Electrically Small Antenna

FBW Fractional Bandwidth

FSRR Folded Split Ring Resonator

PEC Perfect Electric Conductor

PLA Polylactic Acid

SNF Spherical Near-Field Scanner

TEM Transverse Electromagnetic

VNA Vector Network Analyser

WSN Wireless Sensor Network

Chapter 1

Introduction

1.1 Background

Rhinoceros poaching was declared a National Priority Crime in 2014 by the Department of Environmental Affairs in South Africa. This was in response to the exponential increase in poached African Rhinoceros which totalled 1215 for that year in South Africa alone [1].

To assist in combatting this, an animal-borne behavioural monitoring system (ABBMS) prototype was developed at Stellenbosch University in 2016 [2]. This is a ground-based receiver tracking system. The system uses small tags attached to the rear leg of the rhinoceros, as shown in Figure 1.1. The tags collect GPS and tri-axial accelerometer data, where the latter is used to classify the state of the rhinoceros. On-board classification is performed and the processed data is transmitted periodically via a transmitting antenna to a base station. This data is useful to ecologists and conservationists. In particular, any abnormal behaviour of the animal, suggesting it is in danger, may be noticed and quickly acted upon. The system successfully logged the behaviour and coordinates of live rhinoceros in separate experiments and the coordinates were successfully transmitted to a base station in real-time.

The 'Rhinonet' research group was established at Stellenbosch University with the intent of developing and improving various aspects of the ABBMS [3] [4] [5]. A key priority is to improve the range of successful data transmission. The system was designed to transmit data via a wireless sensor network (WSN)

Figure 1.1: The tracking tag enclosure is shown attached to the back leg of a rhinoceros.

at an operating frequency of 433 MHz. The current proposed implementation of the WSN, which is being refined and improved in a concurrent project by Mr. Wotherspoon, is illustrated in figure 1.2.

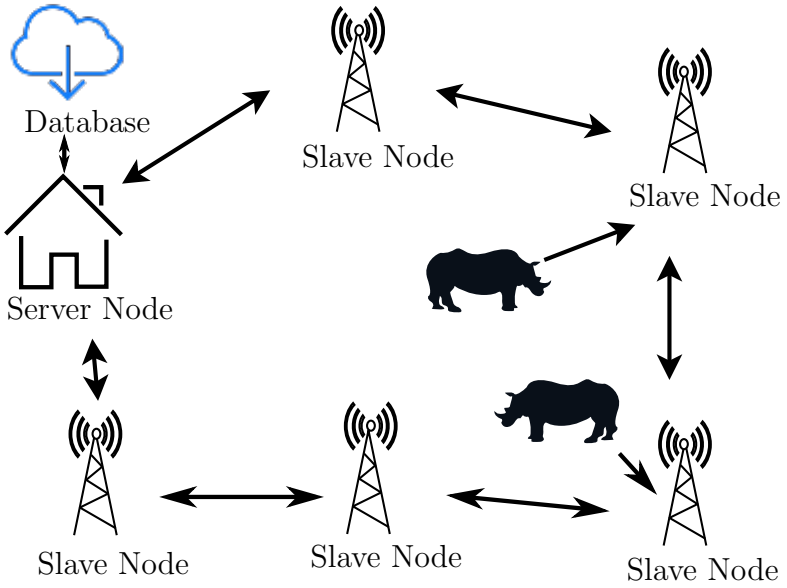

Figure 1.2: An example layout of the WSN. (SOURCE: Image provided by Jonathan Wotherspoon.)

The WSN uses fixed slave nodes, which are scattered about the rhinoceros's monitoring environment, as a path to relay the tag's data to a server node (base

station). The data 'hops' between nodes to find a path to the base station. The base station uploads the received data to a web server for real-time monitoring.

Ideally, the WSN would operate with as few nodes as possible to minimise costs. A lower density of nodes requires transmitted data to travel further. To facilitate this the communication capability of both the tag and node should be improved. The improvement of the node's transceiver is being carried out by Mr. Wotherspoon [6]. This thesis focuses on improving the communication capabilities of the animal-borne tag by designing an improved transmitting antenna.

The antenna is responsible for the efficiency at which available power is converted to radiated power. Given that the energy reserves of the tracking tag are finite, it is important that this efficiency is high. The antenna also directs the radiated power. For this application the orientation of the rhinoceros is unknown, so the antenna should be designed to uniformally radiate its energy.

The enclosure will be subjected to physically harsh conditions. To prevent damage to the antenna it should be completely encased in the enclosure. The size of wavelength that must be transmitted by the antenna at the 433 MHz operating frequency is much larger than the size of the enclosure. The system currently employs a quarter-wave monopole antenna to transmit data from the tag. The antenna is too long to fit inside the enclosure without being bent and this negatively affects its performance. Generally, the limited size of the enclosure places fundamental performance limits on the antenna.

To achieve the goal of designing an improved small transmitting antenna that meets the performance requirements, a careful, systematic approach to its selection and design is required.

1.2 Project Objectives

The project objectives are therefore given as follows:

- To identify the key parameters and the associated values that the improved antenna must satisfy.
- To assess several antenna designs from the literature, including the currently used bent monopole, and select one that best satisfies the requirements.
- To design an optimised prototype of the selected model using FEKO EM simulation software and to construct it for validation.
- To compare the optimised prototype to the equivalent model from the literature.
- To adapt the antenna topology to conform to the size of the sensor enclosure, using FEKO EM simulation software, whist maintaining the performance characteristics, where possible.
- To construct the adapted model to validate performance.
- To compare the performance of the adapted model to the initial optimised prototype model.
- To measure the performance of the adapted model inside the animal-borne sensor enclosure and in close proximity to a human body.

1.3 Project Overview

- Chapter 2: The literature review describes the antenna parameters that will be used to asses the antenna's performance. The limitations of electrically small antennas (ESAs) are highlighted, followed by methods to deal with these limitations. The required antenna parameters are then given and ranked in terms of priority for the specific application. A selection of candidate antennas are then critically examined, with a single model chosen that best satisfies the prioritised requirements. The chosen antenna is the folded split ring resonator (FSRR) antenna.
- Chapter 3: The FSRR antenna's fundamental operation characteristics are first examined using a simulated FEKO model. The model is then

optimised, constructed and validated. The constructed model is subsequently compared to a similar model from the literature.

- Chapter 4: The effects of systematically adapting the antenna's form and shape to fit inside the enclosure are examined. The resulting antenna's input impedance is then tuned for low mismatch. The model is constructed and evaluated against the first prototype. Finally, the model is placed inside the enclosure and in close proximity to a human hand, and the effect on its reflection coefficient is examined.

- Chapter 5: The thesis ends with conclusions and recommendations.

Chapter 2

Literature Study

2.1 Introduction

This chapter begins with an overview of the antenna parameters that will be relevant to our design. Following this, the limits that the antenna's small electrical size places on these parameters will be discussed. Techniques to overcome these limitations will then be explored. Finally, the priority of the antenna requirements for the specific application will be outlined.

2.2 Radiation

An antenna is designed to transmit or receive power in the form of electromagnetic radiation. This thesis will consider the antenna in the transmitting mode.

2.2.1 The Far-Field

It is desirable to determine this radiated power at a specific point in space. To enable this, a coordinate system is defined with the antenna placed at some point in the system. In this thesis, the antenna is always placed at the origin and either the Cartesian or circular coordinate system will be used. An axes representing both coordinate systems with a dipole in the centre is shown in Figure 2.1. Using the circular coordinate system a point in space may be described by (r, θ, φ), where r is the distance from the origin, θ is the angle from

the positive z-axis and φ is the angle from the positive x-axis.

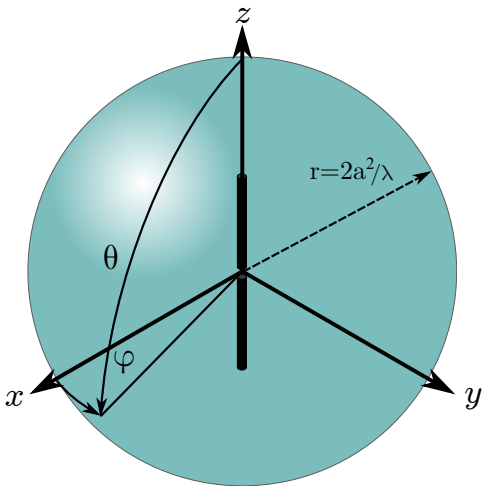

Figure 2.1: Coordinate system with Cartesian and spherical variables. The antenna far-field is represented by the turquoise sphere.

The turquoise sphere surrounding the dipole represents the far-field sphere which is located at $r = 8a^2/\lambda$. Here, a is the radius of the smallest fictitious sphere that totally encapsulates the antenna and λ is the wavelength at the operating frequency. The far-field sphere indicates the distance at and beyond which the radiated waves from the antenna propagate with a planar wave-front. Within this sphere is the radiating near-field and reactive near-field which will be described in more depth in Section 2.4. Importantly, provided the field propagates through free space, the angular (θ, φ) direction of radiated energy does not vary with distance r in the far-field [7]. This makes the radiation behaviour predictable over large distances, so field values are generally taken in the far-field.

2.2.2 Directivity, Gain and Realised Gain

To calculate the total real, or radiated power P_{rad}, the radiation intensity $U(\theta,\ \varphi)$ is integrated over the far-field sphere. The radiation intensity is the power per unit solid angle. The unit of solid angle is the steradian which is the 3-dimensional analogue for the planar radian.

Typically, antennas radiate more strongly in some directions than others. These are known as directional antennas. For the special case of an isotropic radiator, which may only exist in theory, the radiation intensity is equal in all directions. By integrating this constant value U_{iso} over the far-field sphere, the radiated power is determined to be

$$P_{rad} = U_{iso} 4\pi. \tag{2.1}$$

Which gives U_{iso} as

$$U_{iso} = \frac{P_{rad}}{4\pi}. \tag{2.2}$$

The directivity of an antenna is simply its radiation intensity normalised to that of an isotropic antenna radiating the same amount of power

$$\begin{aligned} D(\theta, \varphi) &= \frac{U(\theta, \phi)}{U_{iso}}, \\ D(\theta, \varphi) &= \frac{4\pi U(\theta, \phi)}{P_{rad}}. \end{aligned} \tag{2.3}$$

This ratio is generally expressed in dBi which is decibels relative to an isotropic radiator:

$$D(\theta, \varphi)_{dBi} = 10 \log \left(D(\theta, \varphi) \right). \tag{2.4}$$

The directivity value may be modified to gain or realised gain values by changing P_{rad} in Equation 2.3 to either P_{av} or P_{del}, respectively. To understand these power values, consider the antenna schematic in Figure 2.2. The schematic essentially divides the antenna system into three sections, each with its own associated power. At the antenna terminals a, b the power is delivered P_{del} from the source, via a transmission line. While passing through the terminals, a portion of the power will be reflected. The remaining power is the available power P_{av}. As the available power is converted to radiated power P_{rad}, a portion is lost through Ohmic losses in the conductor and dielectric (if present), or stored. By referencing to P_{av}, the gain is calculated as:

$$G(\theta, \varphi) = \frac{U(\theta, \phi) 4\pi}{P_{av}}. \tag{2.5}$$

This gain accounts for internal losses in the antenna and will hence be smaller than the directivity. By referencing to P_{del}, the realised gain is calculated as:

$$G_{rl}(\theta, \varphi) = \frac{U(\theta, \phi)4\pi}{P_{del}}. \tag{2.6}$$

This realised gain accounts for internal losses and reflection losses and will hence be smaller than the directivity and gain. These losses will be discussed in more detail in Section 2.3.

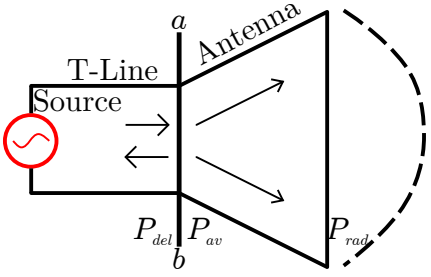

Figure 2.2: Sections of an antenna system and the associated powers.

Each of these radiation functions may be represented on the coordinate system, shown in figure 2.1, as a 3-dimensional radiation pattern. For example, the 3-dimensional directivity pattern of a half-wave dipole is shown in Figure 2.3(a). In this figure, each point θ, φ indicates the distance of the pattern surface from the origin and is proportional to the directivity. The associated colour indicates the value, with red corresponding to high directivity and blue to low. To make the directivity values more easily interpretable a 'cut' is taken through a plane and projected onto a polar plot. In Figure 2.3(a) the red trace corresponds to a cut through $\varphi = 0°$ which is then projected to polar coordinates in Figure 2.3(b). Similarly, the blue trace through $\theta = 90°$ is plotted in Figure 2.3(c).

A vertical cut as in Figure 2.3(b) where θ is the independent value, is an elevation cut. The horizontal cut in Figure 2.3(c), where φ is the independent value, is the azimuth cut. For the elevation cut toward $\theta = 0°$ and $\theta = 180°$, the directivity value becomes very small, indicating a null. Toward $\theta = 90°$ and $\theta = 270°$ (the horizon) the directivity becomes a maximum. Because

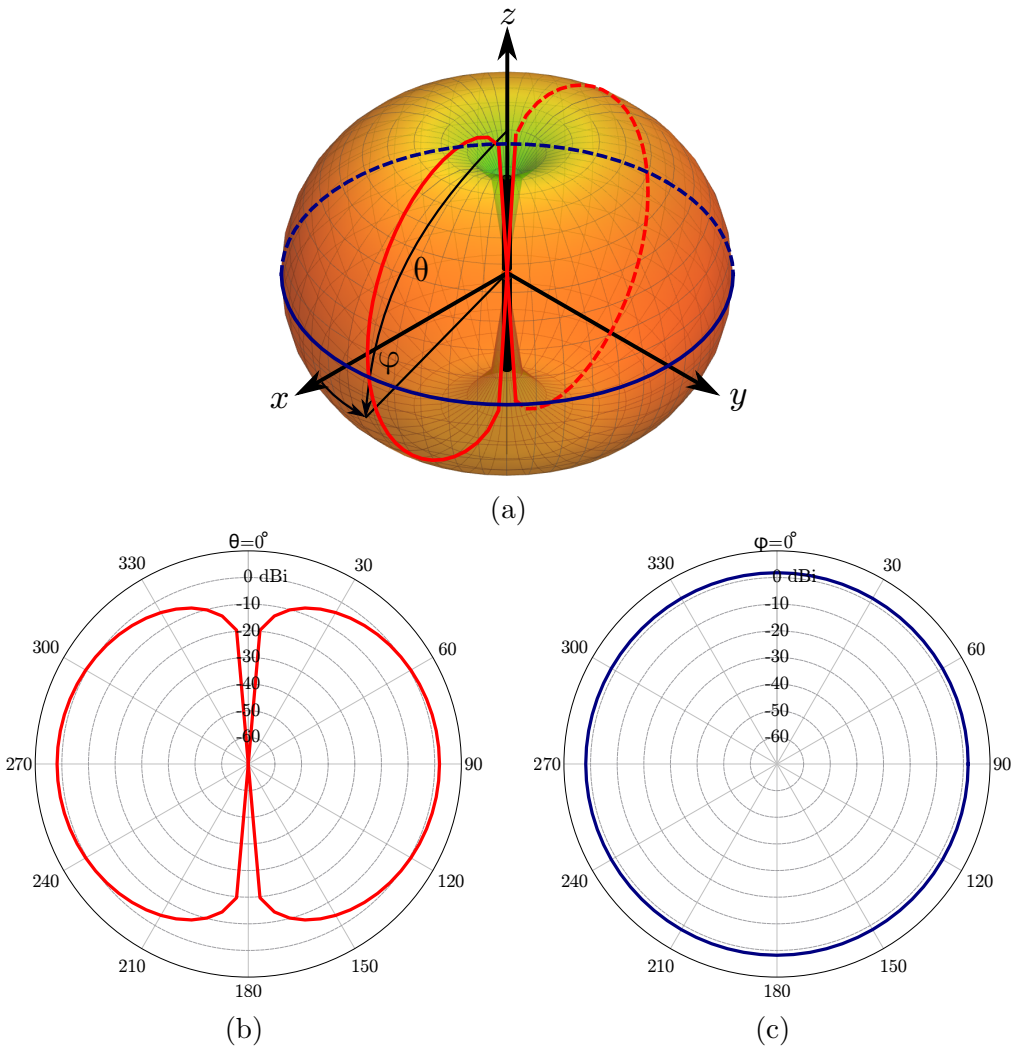

Figure 2.3: In (a): The 3-dimensional directivity plot of a half-wave dipole antenna with the $\varphi = 0°$ and $\theta = 90°$ planes intersecting. The red $\varphi = 0°$ trace in (b) and the blue $\theta = 90°$ trace in (c) are represented on polar plots.

the pattern is uniform in one of the planes, in this case the azimuth plane in (c), the radiation pattern is omnidirectional, rather than directional. For this project the uniform pattern of an omnidirectional antenna would lower the dependence of the signal reception on the rhinoceros's orientation, if the plane containing the uniform cut were aligned parallel to the ground. This would be a useful property. The polar cuts should be chosen so that the 3-dimensional pattern can be recreated from them. For this omnidirectional pattern only the $\varphi = 0°$ and $\theta = 90°$ cuts are needed. Typically, the cuts are chosen to align with the axes.

2.2.3 Polarisation

Electromagnetic waves can be represented as complex vectors consisting of a magnetic H-field and an electric E-field. Each field vector consists of directional components x, y, z in the Cartesian coordinate system and r, θ, φ in the spherical coordinate system. We will consider the spherical coordinate system because it is used more frequently. In the far-field the waves are planar which means they are transverse electromagnetic (TEM). TEM waves lack field components in the direction of propagation. In a spherical coordinate system the waves propagate along the direction of r, so there is no r field component for a propagating wave in the far-field.

If a plane is held perpendicular to the radial direction of the propagating wave in the far-field, the instantaneous electric or magnetic field vector will trace a pattern on it as a function of time [8]. The shape that the electric field traces indicates the type of antenna polarisation for that specific direction. This can be linear, circular or elliptical and corresponds to a line, circle or ellipse pattern traced, respectively. One of the advantages of circular polarisation is the reduction of adverse multipath fading effects [9]. However, circularly polarised antennas are often more complex to create. Hence, this thesis will primarily examine linearly polarised antennas.

Figure 2.4(a) shows the polarisation for a half-wave dipole in a particular direction. The straight blue line traced onto the perpendicular plane indicates linear polarisation. The direction of this line gives the polarisation direction. Here, the field is $\hat{\theta}$ directed. If no point is specified then the antenna polarisation is given by the polarisation in the direction of maximum directivity [10]. For the half-wave dipole this is toward the horizon, where the polarisation is still $\hat{\theta}$ directed.

For maximum power transfer, it is important that the receive and transmit antennas polarisation pattern type and direction is matched, where possible. Figure 2.4(b) shows the $\varphi = 0°$ cut of a dipole antenna attached to a rhinoceros. The dipole is radiating toward a receive antenna with arbitrary radiation pattern. Each of the grey circles represents the antenna's far-field. The polarisation of the transmit antenna at a specific point on the far-field

is linear, and $\hat{\theta}$ directed. If the polarisation of the receive antenna at the point of interception of its far-field is in the same direction as the received wave, as is the case here, then maximum power is transferred. The greater the misalignment of these components, the lower the power transfer.

Figure 2.4(b) also indicates that the antenna's maximum radiation should preferably be directed away from the ground and leg of the rhinoceros.

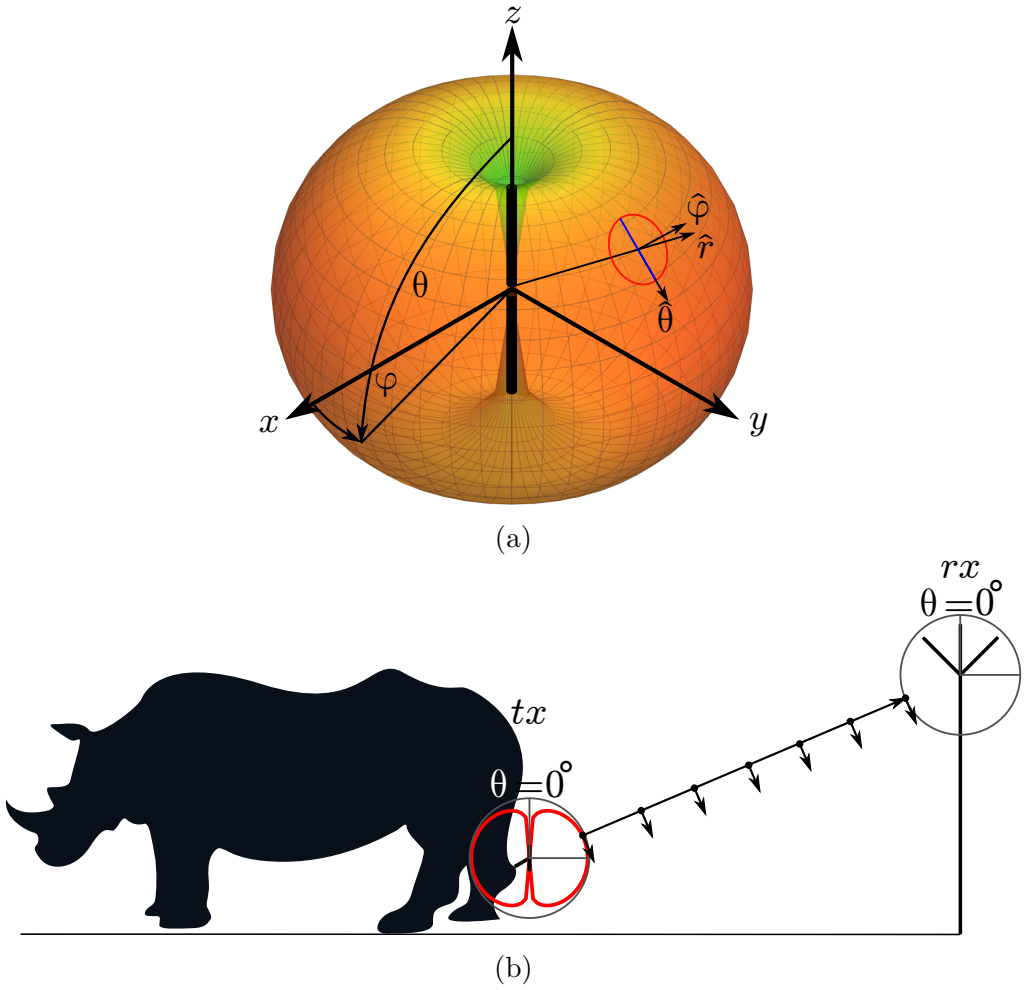

Figure 2.4: In (a): the polarisation pattern of a dipole antenna. In (b): the polarisation match between a dipole antenna attached to a rhinoceros and an arbitrary receive antenna.

2.2.4 The Friis Transmission Equation

The Friis transmission equation gives the relationship between receive and transmit power in a communication system. The system consists of a receive and transit antenna, operating at a distance r apart from each other, which transmit and receive signals of wavelength λ. The transmitted power P_t is the power supplied to the antenna by a source. The receive power P_r is the power received at a load. Assuming that the antennas are matched for polarisation and ignoring any ground reflections the equation is given as follows:

$$P_r = G_{r,rl} G_{t,rl} \left(\frac{\lambda}{4\pi r} \right)^2 P_t. \tag{2.7}$$

The term $\left(\frac{\lambda}{4\pi r}\right)^2$ is the free space loss factor and, as the name suggests, it determines the power lost due to the distance that the propagating wave travels in free space. The realised gain of the receive and transmit antennas is given by $G_{r,rl}$ and $G_{t,rl}$, respectively.

The equation may be rearranged to indicate the distance of successful signal transmission r in free space, given the sensitivity of the receiver. The sensitivity is the minimum received signal power P_r required for the receiver to correctly interpret messages. The equation is rearranged as follows:

$$r = \frac{\lambda}{4\pi} \sqrt{\frac{G_{r,rl} G_{t,rl} P_t}{P_r}}. \tag{2.8}$$

Equation 2.8 indicates that r may be increased by increasing the realised gain of the transmitting antenna. For our application, the use of the free space propagation constant is unreliable because the antenna will be operating in a complex environment. More complex propagation models modify the free space loss factor to account for vegetation, terrain and atmospheric effects [11]. Incorporating these models is beyond the scope of this project. Therefore, equation 2.8 merely serves to illustrate that an increased realised gain from the transmitting antenna will lead to an improvement in transmission distance r, which is one of the goals of this project.

2.3 Efficiency

For situations in which power is limited, such as this project, it is essential that the power provided to the antenna is efficiently converted to radiated power.

The different stages of the antenna and its associated powers P_{del}, P_{av} and P_{rad} were discussed in Section 2.2. The ratios of these powers may be converted into efficiencies

$$e_{ref} = \frac{P_{av}}{P_{del}}, \tag{2.9}$$

$$e_{rad} = \frac{P_{rad}}{P_{av}}, \tag{2.10}$$

$$e_{tot} = e_{ref} e_{rad}. \tag{2.11}$$

Where e_{ref} is the reflected efficiency, e_{rad} is the radiation efficiency and e_{tot} is the total efficiency. The following section discusses these efficiencies in more detail.

2.3.1 Reflection Efficiency

An antenna's power is delivered to its terminals by a transmission line P_{del}, shown in Figure 2.5(a). When the source is sinusoidal the energy propagates through the line as a travelling wave. The voltage amplitude of the wave, travelling away from the source, is V^+. The amplitude is governed by the characteristic impedance Z_0 of the line, which is constant. The wave continues until it reaches the antenna's terminals a, b. At the terminals, if the input impedance Z_A (the impedance seen looking into the antenna) is greater than the characteristic impedance, $Z_A \neq Z_0$, then a portion of the wave is reflected back toward the source with an amplitude V^-. The ratio of the forward travelling, or incident wave, to the reflected wave is the reflection coefficient:

$$\Gamma = \frac{V^-}{V^+}, \tag{2.12}$$

which is also given by

$$\Gamma = \frac{Z_A - Z_0}{Z_A + Z_0}. \tag{2.13}$$

Generally, the reflection coefficient is expressed as a magnitude in terms of decibels,

$$\Gamma_{dB} = 20 \log |\Gamma|. \tag{2.14}$$

To minimise Γ, Equation 2.13 indicates that the antenna impedance Z_A should equal the characteristic impedance Z_0. For this project $Z_0 = 50\ \Omega$, so the antenna should be designed to match this. This can be done in part by designing

the antenna to resonate at the desired frequency f_{res} (where the imaginary impedance component $X_A = 0\ \Omega$) as well as by leveraging tuning parameters (to be discussed in Section 2.4.3) to manually adjust Z_A. The frequency for which Γ is minimum generally coincides with, or is at least very close to f_{res}. Because reflection coefficient versus frequency plots will be examined often in this thesis, the term f_{res} will refer to the frequency of minimum Γ; unless stated otherwise, in which case it will refer to the frequency at which the imaginary antenna impedance component $X_A = 0\ \Omega$.

The frequency range over which $\Gamma <= -10\ dB$ is referred to as the $-10\ dB$ bandwidth. This may be expressed as the fractional bandwidth (FBW)

$$FBW = \frac{f_{upper} - f_{lower}}{f}. \tag{2.15}$$

Here, f_{upper} is the upper frequency where $\Gamma = -10\ dB$ and f_{lower} is the lower frequency where $\Gamma = -10\ dB$. For this project the antenna is only required to operate over an $FBW = 0.4\%$.

To calculate e_{ref} from Γ Equation 2.12 may be converted to a real power ratio of reflected and incident power, where both powers are taken over the same load:

$$\frac{|V^-|^2}{|V^+|^2} = |\Gamma|^2\,. \tag{2.16}$$

The reflection efficiency is then

$$e_{ref} = 1 - |\Gamma|^2. \tag{2.17}$$

2.3.1.1 Baluns

For this project a coaxial cable will be used to deliver power to the antenna terminal. This line is unbalanced; it consists of a single conductor and a return line. The travelling wave inside the coaxial cable swings relative to the grounded return line, which is also the system ground (i.e. the earth of the voltage source to which the transmission line is attached). Many antennas are balanced structures, consisting of two conductors, each carrying signals of equal amplitude that are 180° out of phase.

The balun is a network device attached between the unbalanced coaxial cable and balanced antenna terminals. It isolates the antenna terminals from

the signal ground, preventing currents from returning along the outside of the coaxial cable and causing unwanted radiation. These are called common-mode currents.

Some of the antennas that will be considered will require baluns to operate. Balun's occupy appreciable volume and this should be considered when designing the antenna in view of the project's stringent space constraints.

2.3.2 Radiation Efficiency

To build an intuitive understanding of internal antenna losses the antenna is represented by a Thevenin equivalent circuit, which is depicted in Figure 2.5(b) [12]. The antenna load is attached via a short transmission line to a Thevenin source. The power which was not reflected at the terminals of the antenna is the available power P_{av}. This power is delivered to the input of the antenna with impedance Z_A which is given by

$$Z_A = R_A + jX_A, \tag{2.18}$$

and

$$R_A = R_{loss} + R_{rad}. \tag{2.19}$$

In Equation 2.19 R_{loss} accounts for Ohmic losses and R_{rad} accounts for dissipation by radiation. The imaginary component X_A accounts for energy stored by the antenna. If a current I, supplied by the source, passes through the antenna then the real dissipated powers are given by

$$P_{loss} = |I|^2 R_{loss}, \tag{2.20}$$

$$P_{rad} = |I|^2 R_{rad}. \tag{2.21}$$

The radiation efficiency is the radiated power divided by the available power

$$e_{rad} = \frac{P_{rad}}{P_{rad} + P_{loss}}, \tag{2.22}$$

which can be reformulated using Equations 2.21 and 2.20 to obtain:

$$e_{rad} = \frac{R_{rad}}{R_{rad} + R_{loss}}. \tag{2.23}$$

To maximise the radiation efficiency it is evident that R_{loss} should be kept to a minimum. This can be achieved by primarily using low loss conductors and dielectrics. It should be noted that when lossy dielectrics are added the radiation resistance cannot be represented in series with the loss resistance, so the circuit and Equation 2.23 no longer hold. Regardless, the model presents a foundation for explaining the behaviour of antenna impedance.

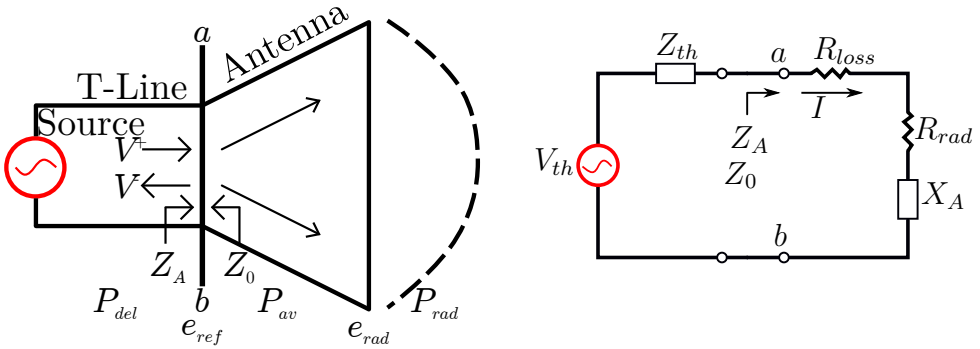

Figure 2.5: An antenna system with the transmission line and source is shown in (a) with associated efficiencies. In (b), the Thevenin circuit representation of the system.

2.3.3 Summary

The gain and realised gain from Equations 2.5 and 2.6 may be represented by scaling the directivity by the radiation efficiency and total efficiency, respectively:

$$G(\theta, \varphi) = e_{rad} D(\theta, \varphi), \tag{2.24}$$

$$G_{rl}(\theta, \varphi) = e_{tot} D(\theta, \varphi). \tag{2.25}$$

The realised gain is then the most practical measure of radiation as it takes into account the reflection and radiation losses. In the design chapters of this thesis, the antenna impedance values will be used to calculate e_{ref} and the radiation efficiency e_{rad} will be extracted directly from simulation or measurement. The total efficiency e_{tot} will then be calculated from these values. For the comparisons with constructed antennas, as well as certain simulation comparisons, the directivity polar plots will be analysed and then equated to

maximum and minimum realised gains, using the corresponding e_{tot} values.

2.4 Electrically Small Antennas

This project will primarily focus on electrically small antennas. The wavelength at the 433 MHz operating frequency is 692.36 mm which is much larger than the maximum dimension of the tag enclosure. It was decided that the antenna should be contained within the enclosure because exposing it would create the risk of damage. Therefore, the final antenna design will be electrically small.

2.4.1 The Near-Field

Within the far-field are the reactive near-field and the radiating near-field. The radiating near-field is located between the far-field boundary and the reactive near-field boundary, although it may not exist for electrically small antennas [13]. An electrically small antenna (ESA) is an antenna that is completely enclosed by its near-field [14]. The radius of the reactive near-field (referred to as simply the near-field from here on) of an electrically small antenna is given by the radianlength [15]

$$rl = \lambda/2\pi, \tag{2.26}$$

which is the inverse of the free space wave number

$$k = 2\pi/\lambda. \tag{2.27}$$

Within this region electromagnetic energy is predominantly stored. It oscillates around the antenna but does not break away to propagate through the environment. A representation of the near-field region of a dipole is shown by the red sphere in Figure 2.6. The relative size of an antenna is the ratio of the radius a of the smallest sphere that encloses it, as depicted in Figure 2.6, to the radianlength

$$ka = \frac{a}{rl} = a\frac{2\pi}{\lambda}. \tag{2.28}$$

In Figure 2.6 the antenna is smaller than the surrounding near-field field so $ka < 1$. The relative size is used as a figure of merit in electrically small an-

tenna design.

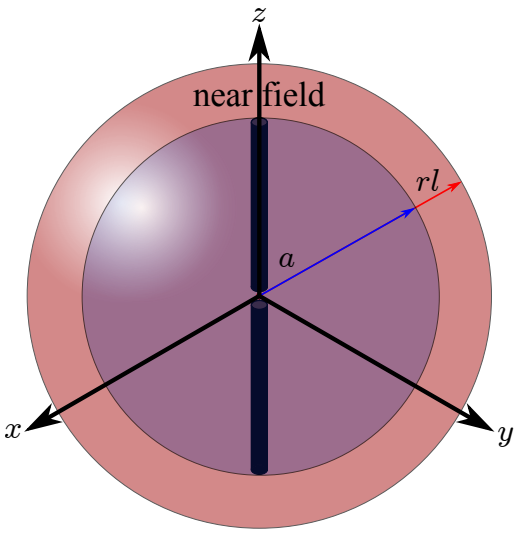

Figure 2.6: An electrically small dipole antenna surrounded by its reactive near-field in red. The blue sphere is the smallest sphere that can completely enclose the antenna, its radius is a.

For this project the antenna will operate in close proximity to a rhinoceros's body. The presence of the rhinoceros tissue within the near-field is anticipated to generally have detrimental effects on the antenna performance. Studies of the performance of two planar antennas when in close proximity to a human body were conducted by Tuovinen et. al [16] [17]. It was shown that total efficiency and hence the maximum realised gain decreased with increasing proximity to the tissue. At low frequencies, the resonant frequency f_{res} also decreased. This could potentially be taken advantage of to further miniaturise the antenna. The effect of the presence of the enclosure and human tissue in the designed antenna's near-field will be examined for this project in chapter 4.

2.4.2 Limitations of Electrically Small Antennas

When designing an ESA it is worth bearing in mind that the small electric size limits its performance. Most significantly for this project the low Q-factor and high f_{res} makes good impedance matching difficult to achieve. The quality

factor Q of an antenna indicates the ratio of stored energy to radiated power per period [18]:

$$Q = \begin{cases} \frac{2\omega W_e}{P_{rad}}, & \text{if } W_e > W_m \\ \frac{2\omega W_m}{P_{rad}}. & \text{if } W_m > W_e \end{cases} \tag{2.29}$$

W_e and W_m are the time-average stored, non-propagating electric and magnetic field energies respectively, ω is the angular frequency $\omega = 2\pi f$ and P_{rad} is the radiated power. For an antenna, it is desirable to achieve low Q so that the power supplied to the antenna is radiated rather than stored. However, the size of an ESA limits the lower bound of its achievable Q-factor. An approximation for the minimum Q as a function of relative size ka for a general omnidirectional antenna was first given by Chu [19]. This formula was inaccurate for antennas whose size approached their radianlength, i.e. $ka \approx 1$. Thus, it was later revised by McLean to an exact formula applicable to antenna's of any radiation pattern of linear or circular polarisation [14]. The relationship is given as follows:

$$Q = \begin{cases} \frac{1}{k^3a^3} + \frac{1}{ka}, & \text{linear polarisation.} \\ \frac{1}{2}\left(\frac{1}{k^3a^3} + \frac{2}{ka}\right), & \text{circular polarisation.} \end{cases} \tag{2.30}$$

This is the lower limit of Q for any antenna of a given size and no practical design has yet reached it.

For both cases the minimum Q increases rapidly for smaller ka by the dominant $\frac{1}{k^3a^3}$ factor. This means that for a given amount of power available to the ESA, a small percentage will be radiated. Equation 2.21 indicates that low P_{rad} equates to low R_{rad} which limits the matching capability of the antenna.

The matching problem is exacerbated by the increase in f_{res} that accompanies a decrease in physical size. This is expressed by the frequency scaling theorem which states that an antenna's resonant frequency f_{res} scales inversely to its physical dimensions, provided all material parameters remain the same [20]. So, if an antenna resonates at a particular f_{res}, and its physical dimensions are doubled (scaled by a factor of 2) then its f_{res} will halve. The theory also maintains that the scaled antenna will display identical efficiencies, directivity and radiation pattern to the non-scaled antenna at the respective f_{res}.

This will be exploited during the measurement phase of the project.

A high Q-factor also corresponds to a narrow fractional bandwidth. Given that the channel bandwidth for this project is only 0.4% a narrow bandwidth is acceptable. Both Harrington and Chu describe maximum directivity limits corresponding to ka, Chu for omnidirectional antennas and Harrington for general antennas [18] [19]. The solutions require an understanding of spherical wave functions which is beyond the scope of this thesis. But it should still be noted that an ESA has an upper limit to its maximum achievable directivity.

2.4.3 Impedance Modification Techniques

The low R_{rad} and high f_{res} inherent to ESAs may be increased and decreased, respectively by manually modifying certain antenna parameters, known as tuning parameters. Alternatively, an external tuning network may be added between the source and antenna to present a matching impedance to the transmission line.

2.4.3.1 Real Impedance

For a half-wave dipole antenna the input impedance may be increased by adding a parallel arm. The modification is shown in Figure 2.7.

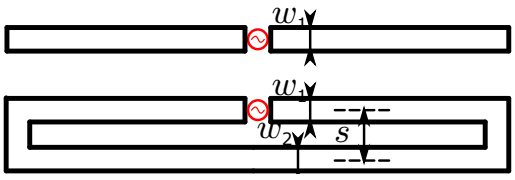

Figure 2.7: Schematic of the folded half-wave dipole. The added parallel arm increases the dipole input impedance Z_d by a factor of 4.

Provided $s << \lambda$ the magnetic coupling between the arms causes the antenna's impedance to increase by a factor of 4 [21]

$$Z_A = 4Z_d. \tag{2.31}$$

In Equation 2.31, Z_d is the input impedance of a standard half-wave dipole. Given that the antenna is at resonance, the increased Z_A will predominantly raise the input resistance R_A. By increasing the $w2/w1$ conductor ratio above

unity the factor by which Z_d increases is raised proportionately [22]. This will be examined further in section 3.2.

2.4.3.2 Imaginary Impedance

By decreasing the frequency at which $X_A = 0\ \Omega$ the resonant frequency may be decreased. One technique is to surround the antenna with a high relative permittivity ϵ_r dielectric which causes the antenna to become a slow wave structure [23]. This technique is known as dielectric loading. Here, the higher ϵ_r of the dielectric causes the wavelength of the antenna's currents to increase which lowers the frequency of resonance.

Alternatively, the antenna inductance L or capacitance C may be influenced to lower f_{res}. An ESA may be represented as a RLC circuit [24]. For simple ESAs this may either be a series RLC or parallel RLC circuit. In both cases the f_{res} is related to L and C by

$$f_{res} = \frac{1}{2\pi\sqrt{LC}}. \tag{2.32}$$

By increasing the antenna L and C values the f_{res} may be lowered. This can be achieved by modifying the antenna's geometry. For example, the electrically small monopole is represented as a series RLC circuit. By winding the monopole conductor into a helical shape, the inductance increases and f_{res} decreases. In this thesis some of the examined antennas will be represented by a combination of series and parallel RLC circuits. In this case Equation 2.32 does not hold exactly and experimentation will be required to determine how the antenna capacitance or inductance can be changed to lower f_{res}.

2.4.3.3 Matching Networks

By adding lumped element or microstrip 'stubs' between the source and antenna, the input impedance may be transformed to the characteristic line impedance. These external networks will introduce additional losses and, especially in the case of microstrip stubs, will occupy more surface area.

2.5 Project Requirements

Now that the antenna parameters have been defined, the required values for the project will be given. These will be ranked in terms of importance to facilitate subsequent comparisons between suitable antennas, presented in Section 2.6.

Ideally, a comprehensive analysis of the communication link would have been established to determine the exact antenna requirements for the system to function correctly. For a simple point-to-point communication system in free space, Equation 2.7 could be used to calculate the required realised gain. This technique would not prove sufficient for our system which is mobile and situated in a harsh, complex environment. Characterising the system would require a significant time investment and is beyond the scope of this project. Alternatively, required parameters may be chosen by assessing industry standards and the performance of commonly used antennas. Limitations to the antenna's required parameters due to its electrically small size may also be taken into account, although the main limitation here is bandwidth, which may be narrow for our application. The parameters are then defined as follows:

1. The antenna should exhibit low mismatch at 433 MHz. Typically, reflection coefficient values are designed to be $\Gamma \leq -10\ dB$, with $\Gamma \leq -20\ dB$ being more desirable. This corresponds to reflection efficiencies of $e_{ref} \geq 90\%$ and $e_{ref} \geq 99\%$ respectively.

2. The antenna must fit inside the enclosure whose maximum inner dimension is 126 mm which corresponds to a relative size of $ka = 0.57$ at 433 MHz. The antenna ka should be at least as small as this value. It should be noted that achieving this relative size will not necessarily mean that the antenna will fit inside the enclosure. If the antenna is circular with $ka = 0.57$ at 433 MHz the narrow width of the rectangular enclosure will prevent the antenna from fitting. Therefore, whether the antenna fits will depend on its shape, and this should be taken into consideration.

3. The radiation efficiency should be $e_{rad} \geq 80\%$. Wire antennas may

achieve e_{rad} values greater than 90%, even if they are ESAs. However, it is anticipated that dielectric loading will be used to achieve a low f_{res} at a small relative size. Lossy dielectrics may need to be used to keep costs down and this will reduce the e_{rad} value below 90%. Hence, the required e_{rad} is lower than the required e_{ref}.

4. The total required efficiency is then $e_{tot} \geq 79.2\%$.

5. To further help achieve matching at this size the antenna should have its own tuning parameters available.

6. The pattern should be omnidirectional, with the uniform plane parallel to the physical ground, to remove the dependence of signal reception on the rhinoceros's orientation.

7. The maximum realised gain should be at least $G_{rl,max} \geq 0\ dBi$. This condition means that the exact amount of power delivered to the antenna terminals is radiated in the direction of maximum gain. Of course, it is more desirable for the antenna to amplify the power delivered to it. The half-wave dipole is a commonly used omnidirectional antenna with a maximum realised gain of $G_{rl,max} = 1.95\ dBi$. This value will be used as the preferred requirement for the antenna to achieve.

8. There is a high probability that the enclosure will break when attached to a rhinoceros. The antenna should be a simple structure, made from low cost materials so that it may easily be replaced if it is broken.

9. The polarisation of the antenna is not essential, but it should be noted to determine the polarisation of the receive antenna that will be used for the project.

10. The channel bandwidth is very narrow so the FBW of the antenna only needs to be 0.4%.

The requirements are summarised in table 2.1 with red cells indicating high priority and green low priority.

Table 2.1: Table of requirements for the antenna based on previously discussed parameters. The red rows are highly prioritized; yellow – medium; green – low.

Parameter	Desired Value
ka	≤ 0.57
e_{ref} (%)	≥ 90; $\geq 99\%$ preferable.
e_{rad} (%)	≥ 80
e_{tot} (%)	≥ 72; ≥ 79.2 preferable.
Radiation Pattern	Omnidirectional
Realised Gain (dBi)	≥ 0; ≥ 1.95 preferable.
Inherent Tuning Parameters	Available
Cost/Complexity	Low
Polarisation	Linear/Circular
FBW (%)	≥ 0.4

2.6 Antenna Design Comparison

With the parameter requirements in mind a number of candidate antennas were compared. The antennas were all omnidirectional and their use-cases were similar to that of this project, i.e. they were used in tracking systems, were electrically small or were used in other mobile systems. The most favourable antenna will be selected for use in the project. The antennas' performances were mainly based off of the literature and, where necessary, FEKO simulations.

The relative size of the antennas will be given at their resonant frequency, rather than at 433 MHz. The need for a balun will add to the space requirement of the antenna, so it will be acknowledged whether an antenna needs one or not.

2.6.1 The monopole, dipole and loop antennas

Research literature on the design of transmitting antennas for ground-based receiver tracking systems is scarce. Many of the papers describing the tracking system neglect to mention the type of antenna. Of the papers that do mention the antenna used, the most common is the quarter-wave monopole and the loop antenna [25]–[30]. These antennas will be examined here. The quarter-wave monopole antenna will be attached to a ground plane of a half-wavelength diameter, which is large enough to approximate an infinite ground

plane. The half-wave dipole will also be examined as it is a natural extension of the quarter-wave monopole.

The Rhinonet system currently uses a quarter-wave monopole antenna which is bent to fit inside the enclosure; it is also attached to a small ground plane. This antenna will be simulated to act as a benchmark against which the newly chosen antenna may be compared.

The dipole and straight-wire loop models were acquired from Antenna Magus software package. The simulated models of the straight-wire monopole, dipole, loop and bent monopole antennas are shown in Figures 2.8(a), 2.9(a), 2.10(a) and 2.11(a), with corresponding patterns in Figures 2.8(b) , 2.9(b), 2.10(b) and 2.11(b), respectively. Their important parameters are presented in Table 2.2.

These radiators are cheap to manufacture, although the dipole and loop require a balun. The straight-wire monopole, dipole and loop antennas are all electrically large and suffer from poor mismatch when reduced below their resonant lengths. To compensate, the conductors may be wound to increase inductance and lower f_{res}. The R_{rad} of an electrically small loop may be increased by raising its number of turns or adding a ferrite core to its centre [31].

The radiation patterns of the straight-wire monopole, dipole and loop antennas are 'doughnut-shaped' with the monopole and dipole's maximum radiation toward the horizon and the loop's maximum toward $\theta = 0°, 180°$. The monopole's maximum directivity is greatest here, with $D_{max}(\theta, \varphi) = 2.81\ dBi$. The total efficiency of the loop suffers due to high mismatch with $e_{ref} = 76.92\%$. The large R_A value of the loop is the cause. Despite its low e_{tot} the loop's maximum realised gain is still higher than the dipole due to its directivity of $D_{rl,max} = 2.54\ dBi$.

The bent monopole antenna suffers from high input resistance, due to its decreased height above the ground plane compared to the straight-wire monopole antenna [32]. This results in a very low maximum realised gain $G_{rl,max}$ of $-3.5\ dBi$.

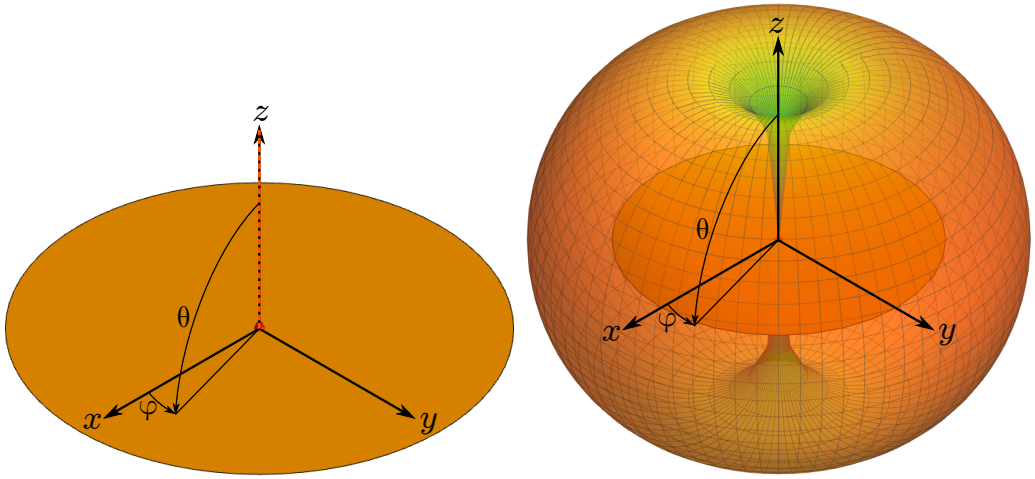

(a) (b)

Figure 2.8: (a) Simulated model of a quarter-wave monopole antenna over a ground plane. (b) 3-dimensional radiation pattern of the quarter-wave monopole antenna.

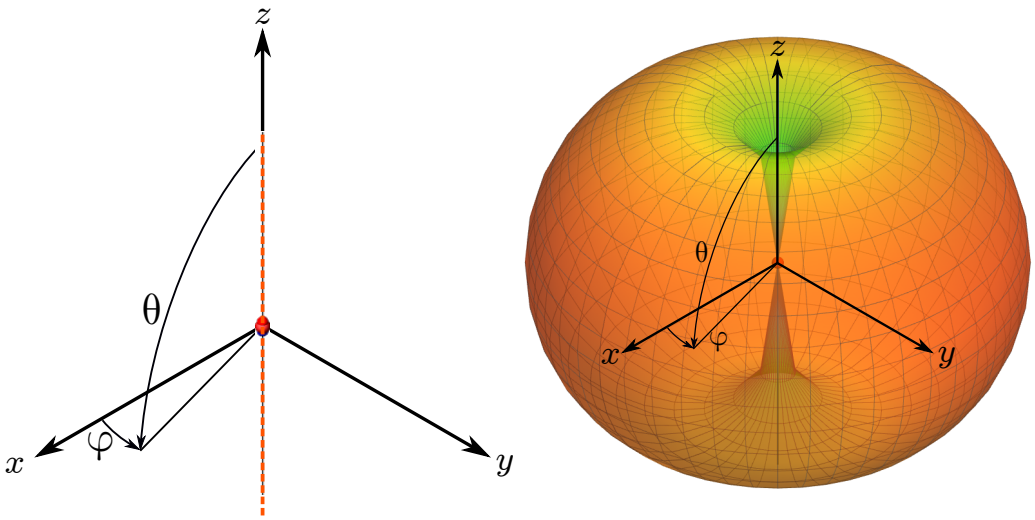

(a) (b)

Figure 2.9: (a) The half-wave dipole antenna model, acquired using Antenna Magus. (b) 3-dimensional radiation pattern of the half-wave dipole antenna.

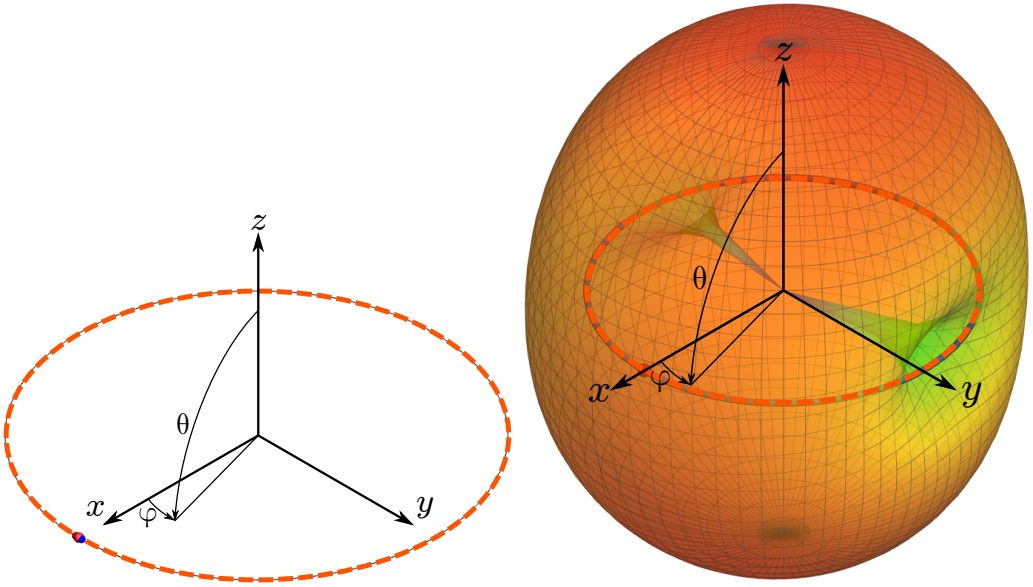

(a) (b)

Figure 2.10: (a) The full-wave loop antenna model, acquired using Antenna Magus. (b) 3-dimensional radiation pattern of the simulated full-wave loop antenna.

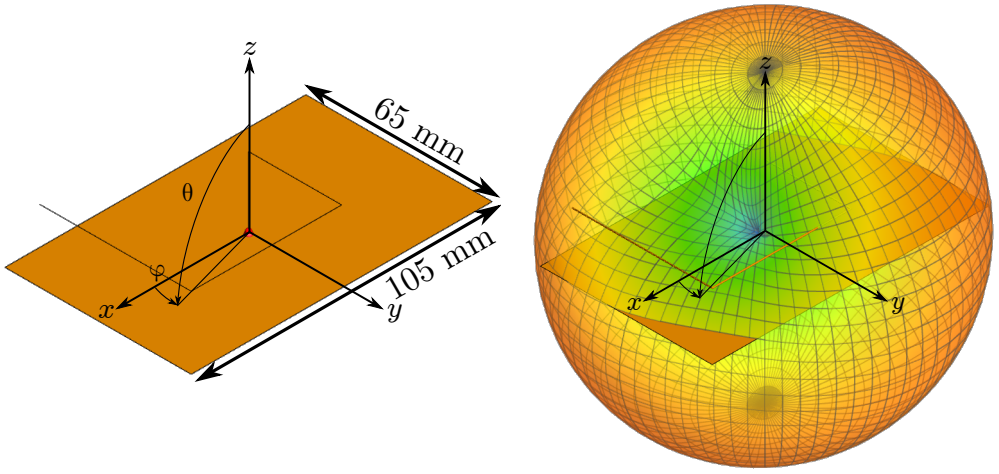

(a) (b)

Figure 2.11: (a) Simulated model of a bent quarter-wave monopole antenna over a small ground plane. The antenna will fit inside the enclosure. (b) 3-dimensional radiation pattern of the bent quarter-wave monopole antenna.

Table 2.2: The parameters of a simulated quarter-wave monopole with a small ground plane, normal helix antenna and small loop antenna.

Parameter	**Monopole**	**Dipole**	**Loop**	**Bent Monopole**
ka	3.25	1.49	1.07	0.70
e_{tot} (%)	98.95	95.89	76.83	28.86
$G_{rl,max}$ (dBi)	2.76	1.95	2.54	-3.5
Tuning Params.	Available	Available	Available	Available
Balun	Not Req.	Required	Required	Not Req.
Cost	Low	Low	Low	Low

2.6.2 The dielectrically-loaded octafilar helix Antenna

The SL3101 octafilar helix antenna is designed for use with the Iridium satellite constellation [33]. It is a patented product and so its parameters were taken from its data sheet. Although this is a satellite-based tracking system the antenna displays favourable properties for our application. Its design is shown in Figure 2.12. The antenna is an extension of the quadrifilar helical antenna, with four helices added. The additional arms increase the radiation efficiency by increasing the conductor surface area [34]. They also create circular polarisation.

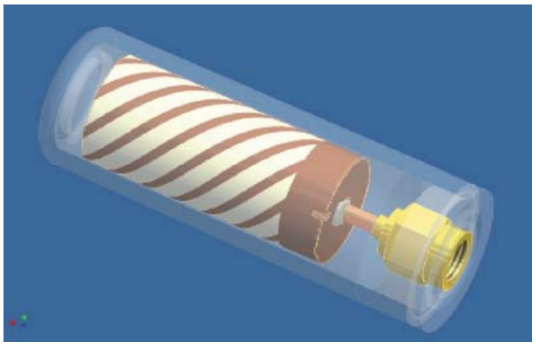

Figure 2.12: Isometric image of the dielectrically loaded octafilar helix antenna. SOURCE: *SL3101 Passive Iridium Antenna Product Specification*, v4, Sarantel, Sep. 2009.

The parameters of the SL3101 octafilar helix antenna are shown in Table 2.3. The antenna incorporates a sleeve balun into the design. The antenna's electrically small size of $ka = 0.61$ is achieved by printing the conductor on a

high permittivity substrate. This specialised process makes the antenna relatively costly. The high ϵ_r substrate constrains the antenna's near-field to a small volume, which lowers the antenna's susceptibility to detuning in the presence of animal tissue.

Its maximum directivity is 2 $dBic$ toward $\theta = 0°$. Here, 'c' in 'dBic' indicates that the reference isotropic antenna is also perfectly circularly polarized. A linearly polarized antenna would lose $3dB$ when its reference is changed from an isotropic antenna, to an isotropic antenna with circular polarization. Unfortunately, the e_{tot} of this antenna is low due to the low radiation efficiency, $e_{rad} = 65\%$. This results in a severely reduced maximum realised gain value of $G_{rl,max} = 0.61\ dBic$.

Table 2.3: The dielectrically loaded octafilar helix antenna parameters.

Parameter	**Helix**
ka	0.61
e_{tot} (%)	60.93
$G_{rl,max}$ $(dBic)$	1.72
Tuning Params.	Not Av.
Balun	Not Req.
Cost	High

2.6.3 The PIFA Antenna

The mobile phone industry is another sector which requires antennas to be placed inside electrically small enclosures. The Planar Inverted F-Antenna is used extensively in mobile phones [35]. A simulated model which was obtained using the Antenna Magus software package is shown in Figure 2.13(a). The design originates from the inverted-L antenna which is essentially a monopole bent parallel to the ground plane [9]. This antenna has low radiation resistance R_{rad}. To match the input impedance a parallel stub is added close to the feed arm, between the antenna and ground. This particular configuration is designed to be parallel to the RF ground plane of the mobile phone [36]. The ground plane underneath the radiating element is cut-away to allow omnidirectional radiation. The substrate loss tangent was equated to 0.017 which

is the same value as FR-4 substrate.

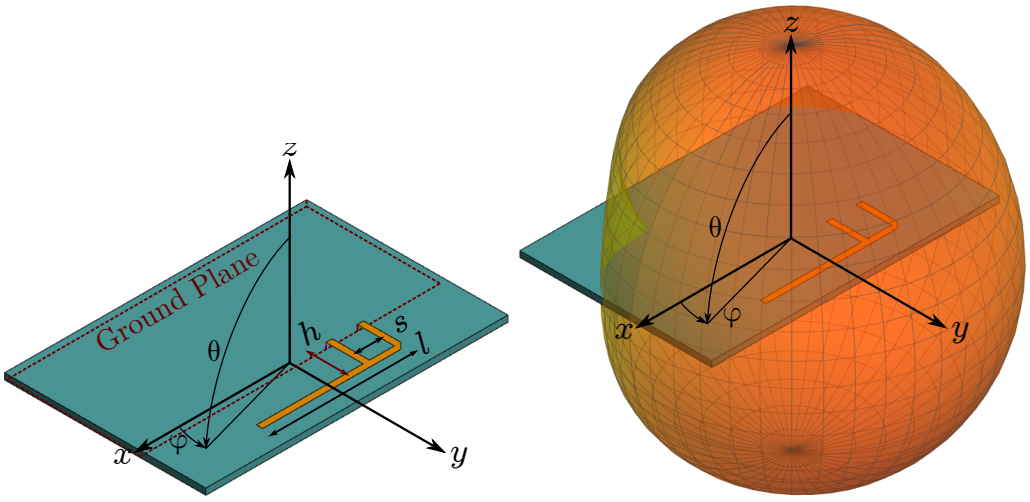

(a) (b)

Figure 2.13: (a) The PIFA antenna model and its parameters, acquired using Antenna Magus. (b) 3-dimensional radiation pattern of the PIFA antenna.

The radiating F-element is small, with dimensions of 23.14×6.97 mm. However, the ground plane and substrate forms part of the radiator, so $ka = 1.44$ which is large. Decreasing the size of the ground plane will cause severe mismatch. Thus, the antenna will not fit inside the enclosure.

The radiation pattern is omnidirectional, although it is slightly disfigured by the ground plane. Maximum directivity is 2.35 dBi toward $\theta = 22.5°, \varphi = 97.5°$. Its high total efficiency $e_{tot} = 94.99$ dBi means the maximum realised gain is close to the directivity $G_{rl,max} = 2.13$ dBi. The antenna is unbalanced and hence does not require a balun. It is cheap, and is easy to manufacture and integrate into existing electronics.

The antenna offers a variety of tuning mechanisms. By increasing the length l the resonant frequency decreases. The gap between the feed and shunt stub s may be decreased to increase R_{rad} and decrease f_{res}. Finally, the proximity of the main arm to the ground plane h may be decreased to increase the input impedance Z_{in}.

Table 2.4: The planar inverted-f antenna parameters.

Parameter	PIFA
ka	1.44
e_{tot} (%)	94.99
$G_{rl,max}$ (dBi)	2.13
Tuning Params.	Available
Balun	Not Req.
Cost	Low

2.6.4 The Folded Split Ring Resonator Antenna

The folded split ring resonator (FSRR) antenna, shown in Figure 2.14(a), is a novel antenna based on the single-arm split ring resonator (SRR), which was conceived as a metamaterial particle [37]. It has since been investigated extensively as an electrically small radiator [38]. More recently, the parallel conductor arm principle of the folded dipole antenna was applied by Kim and Nam to the single-arm SRR antenna to increase its input impedance [39].

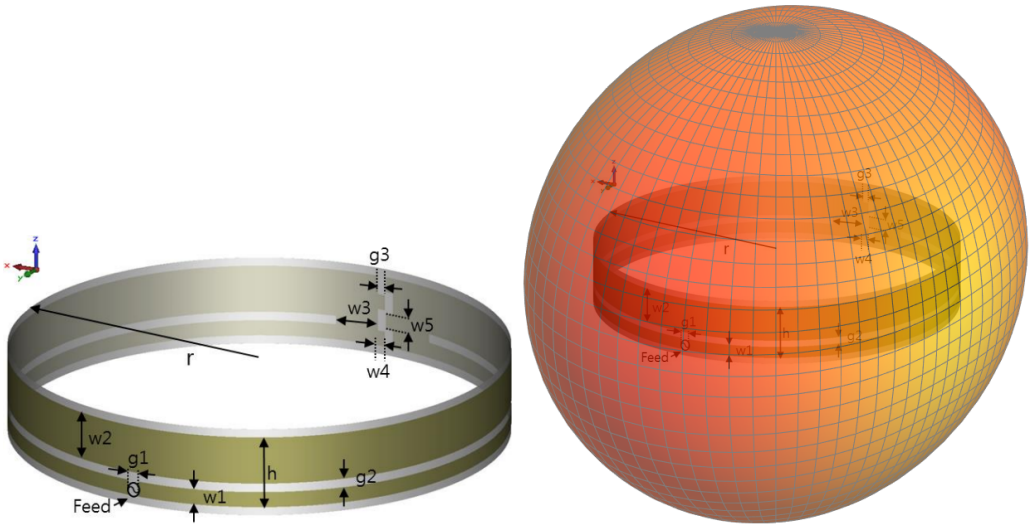

(a) (b)

Figure 2.14: (a) The FSRR antenna model and its parameters. SOURCE: J.-H. Kim and S. Nam, *A Compact Quasi-Isotropic Antenna Based on Folded Split-Ring Resonators*, IEEE Antennas and Wireless Propagation Letters, vol. 16, pp. 294–297, 2017. (b) 3-dimensional radiation pattern of the FSRR antenna.

The antenna parameters presented in Table 2.5 were adopted from Kim's simulated design. The antenna is a balanced structure that resonates at a relative size of $ka = 0.41$. The folded conductor arms increase Z_A allowing R_A to be raised close to 50 Ω. It radiates quasi-isotropically due to the simultaneous excitation of an electric and magnetic dipole. The 3-dimensional radiation pattern shown in Figure 2.14(b) is from an independent simulation with different parameters, done by this project's author. This 3-dimensional pattern should be treated as an approximation to what would be displayed by Kim's model. The values presented hereafter, however, are accurate.

The maximum realised gain is $G_{rl,max} = 2.11\ dBi$ toward $\theta = 105°, \varphi = 0°$. Because the pattern is quasi-isotropic the directivity at the null points is still relatively high $D_{min} = -3.08\ dBi$ toward $\theta = 90°, \varphi = 90°$.

The FSRR has two tuning mechanisms: the capacitance between the conductor ends may be raised to increase f_{res}; the ratio of the top-to-bottom conductor widths w_2/w_1 may be increased to further raise Z_A.

Table 2.5: The folded split ring resonator antenna parameters.

Parameter	**FSRR**
ka	0.41
e_{tot} (%)	91.32
$G_{rl,max}$ (dBi)	2.11
Tuning Params.	Available
Balun	Required
Cost	Medium

2.6.5 Antenna comparison and decision

Table 2.6 shows the combined antenna parameters, with red indicating the parameter is not met and green indicating the parameter is met. For the e_{tot} and $G_{rl,max}$, which have 'base' requirements and 'preferable' requirements, the parameter is coloured green if it satisfies the base requirement. The relative sizes are not highlighted because their values are taken at the examined antenna's resonant frequency, rather than the operating frequency of $f_{res} = 433\ MHz$. This allows the antenna's to be compared to one another in terms of relative

size, but the values cannot be used to determine whether the antenna will fit inside the enclosure. The

Table 2.6: Parameters of the compared antennas.

Params	**Mono**	**Dipole**	**Loop**	**Bent Mono**	**Helix**	**PIFA**	**FSRR**
ka	3.25	1.49	1.07	0.70	0.61	1.44	0.41
e_{tot} (%)	98.95	95.89	76.83	28.86	60.93	94.99	91.32
$G_{rl,max}$ (dBi)	2.76	1.95	2.54	-3.5	1.72	2.13	2.11
Tuning Params	Available	Available	Available	Available	Not Av.	Available	Available
Balun	Not Req.	Required	Required	Not Req.	Not Req.	Not Req.	Required
Cost	Low	Low	Low	Low	High	Low	Medium

The monopole and PIFA antennas require ground planes to function satisfactorily. Decreasing the ground plane sizes to fit inside the enclosure would reduce the antenna performances to unacceptable levels. The loop and dipole antenna are both cheap and simple to construct. However, they are also too large to fit inside the enclosure. Both could conceivably be made to resonate at electrically small sizes by increasing inductance but only the loop offers a mechanism to raise its R_A.

The bent monopole antenna is electrically small but suffers from the lowest e_{tot} and the lowest $G_{rl,max}$. The helix antenna is electrically small but its electrical size is still above the required value of $ka = 0.57$. It is a commercial antenna and hence its input impedance cannot be tuned. Furthermore, its low e_{rad} significantly reduces its maximum realised gain $G_{rl,max}$. The FSRR antenna is the smallest of the antennas and also offers f_{res} and R_{rad} tuning options. The substrate it uses is expensive but could potentially be replaced by affordable FR-4 substrate. It exhibits high realised gain and its radiation pattern is quasi-isotropic. The quasi-isotropic pattern should help reduce reception dependency on the rhinoceros's orientation. The electrically small loop and FSRR antennas are the most favourable candidates. However, the FSRR naturally operates at an electrically small size, whereas the loop's volume would have to be reduced by more than 50%. It may therefore be challenging

to correctly tune the loop. Furthermore, the FSRR antenna's radiation pattern is quasi-isotropic, which means it lacks the nulls of the loop antenna. The performance of the FSRR significantly exceeds the bent monopole, which is the antenna that is currently used. For these reasons, the FSRR was chosen as the antenna architecture for this project.

2.7 Summary and Conclusion

The important antenna parameters that will be used in this thesis were first described. The electrically small antenna (ESA) was then defined. The performance limitations that ESAs face were subsequently examined. It was found that ESAs are defined by high Q-factors, which coincide with low radiation resistance values. They also tend to resonate at high frequencies. These limitations increase the difficulty of matching the antenna's input impedance to the transmission line. Impedance modification techniques were then examined as a means of improving the matching capabilities of electrically small antennas. Following this, the project requirements were defined. The chosen antenna should primarily radiate with an omnidirectional pattern, with high radiation and reflection efficiencies. These requirements should be met while the antenna is electrically small. A group of candidate antennas were then compared to each other to determine which would best satisfy the performance requirements. It was found that the folded split ring resonator antenna (FSRR) antenna was the optimal choice. It exceeded the performance of the bent monopole antenna that is currently being used.

Chapter 3

The Folded Split Ring Resonator Antenna

3.1 Introduction

In the previous chapter, the FSRR antenna was identified as the antenna best suited to our design requirements. This chapter will examine its operating principles and how they relate to the simpler folded dipole antenna. The effectiveness of the antenna's tuning parameters will then be tested. Following this, a simple prototype model will be designed and optimised using the FEKO simulation software. The antenna will subsequently be constructed and its performance measured in order to validate the simulated model. This initial prototype will not necessarily fit inside the animal borne enclosure. Rather, it will be used as a base model which will be adapted to fit inside the enclosure in Chapter 4. Finally, this model will be compared to the literature concerning the FSRR antenna as presented in Chapter 2.

3.2 Fundamental Antenna Operation

To develop an intuitive understanding of the antenna's operation, the properties of the FSRR antenna will be compared to those of a folded half-wave dipole. The folded dipole and FSRR antennas, together with their parameters, are shown in Figures 3.1(a) and (b), respectively. The antennas share the parameters dl, s, w_1 and w_2 which define the antenna length, spacing between the centres of the conductors, the width of the lower conductor and the width

of the upper conductor, respectively.

The FSRR antenna may be interpreted as a folded dipole that has been curled into a circular shape, with a gap of arc length gl between the ends of the conductor. This transformation decreases the electrical size of the antenna but the resonant frequency remains approximately the same.

To illustrate this, a folded half-wave dipole of $dl = 324.98\ mm$, $s = 3.13\ mm$ and $w_1 = w_2 = 1.46\ mm$ was simulated to resonate at approximately $f_{res} \approx 433\ MHz$. The metal used was lossless perfect electric conductor (PEC). This antenna was subsequently curled into the shape of the FSRR antenna, with a gap length of $gl = 12.4\ mm$, and simulated.

The imaginary impedance responses for the two antennas are shown in Figure 3.2(a). Both antenna's traces align close to the resonant frequency (where $X_A = 0\ \Omega$) which is approximately $f_{res} = 433\ MHz$. However, at this frequency the electrical size of the folded dipole is $ka = 1.47$ whereas it is $ka = 0.49$ for the FSRR. This represents a 66.67% decrease in occupied volume.

This decreased ka reduces the radiation resistance of the FSRR antenna, as shown in figure 3.2(b). Because the folded dipole has a high radiation resistance of $R_{rad} = 282.97\ \Omega$ the decrease in R_{rad} of the FSRR actually lowers it to a more favourable $R_{rad} = 47.62\ \Omega$. Hence the FSRR antenna is well matched to a 50 Ω line.

The FSRR antenna radiates with a quasi-isotropic pattern, described in Section 2.6. The pattern is a result of the superposition of a y-directed electric dipole and a z-directed magnetic dipole. These modes of operation may be understood by applying an even-odd mode current analysis to the FSRR antenna. A representation of the currents is shown in Figure 3.3. The even mode currents are represented by the two red arrows which are at a maximum amplitude at the gap and feed and a minimum amplitude near $\pm y$. These currents form a y-directed electric dipole. The odd mode currents are represented by the two blue arrows, which are at a constant amplitude around the entire structure. These form a $\hat{z}$-directed magnetic dipole. The superposition

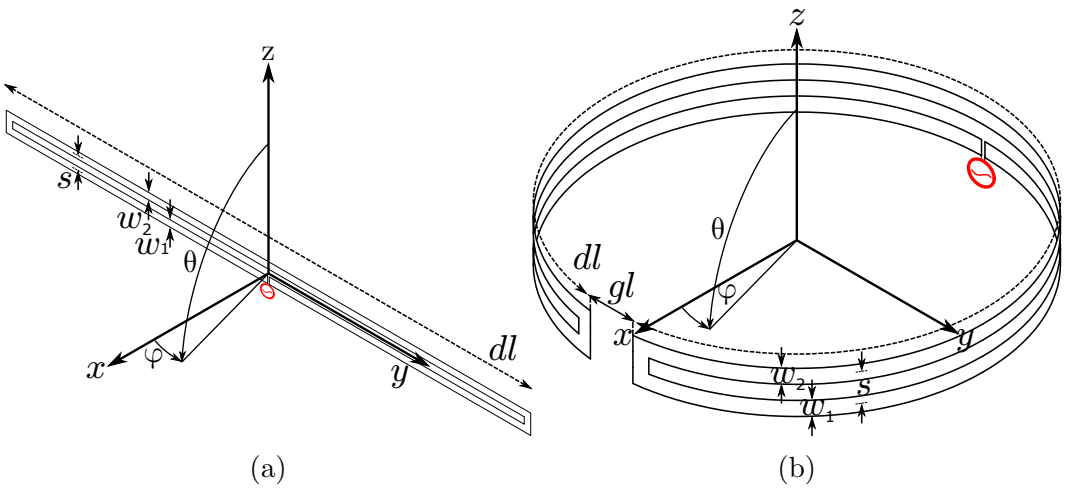

Figure 3.1: The folded dipole antenna from which the FSRR antenna is derived is shown in (a). The resulting FSRR antenna is shown in (b).

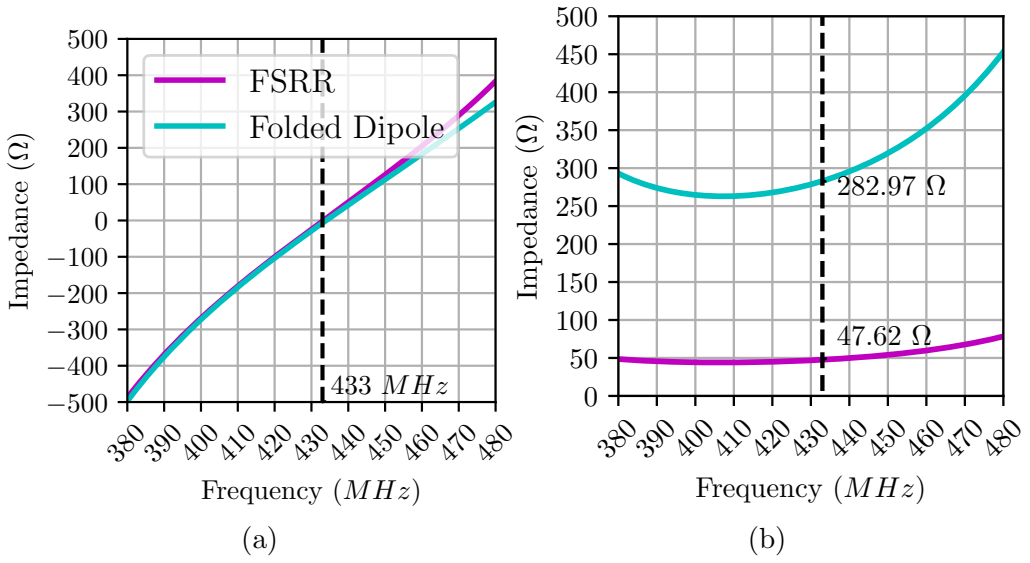

Figure 3.2: The input impedance response of the (a) imaginary component and (b) real component for the folded dipole and FSRR antennas.

of these modes results in the quasi-isotropic radiation pattern.

At each point on the far-field sphere the directivity of the FSRR antenna may be decomposed into its separate θ and φ components and plotted. By doing this the operation of both electric and magnetic dipoles may be demonstrated.

This is done in Figures 3.4(a), (b) and (c) with the $\varphi = 0°$ cut for (a) and

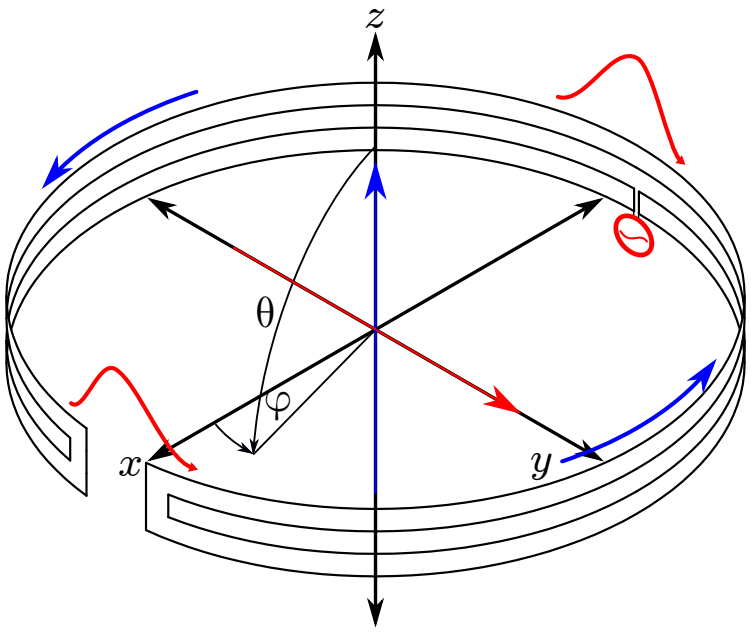

Figure 3.3: An even-odd mode analysis of the currents shows that the FSRR antenna forms a z-directed magnetic dipole and a y-directed electric dipole.

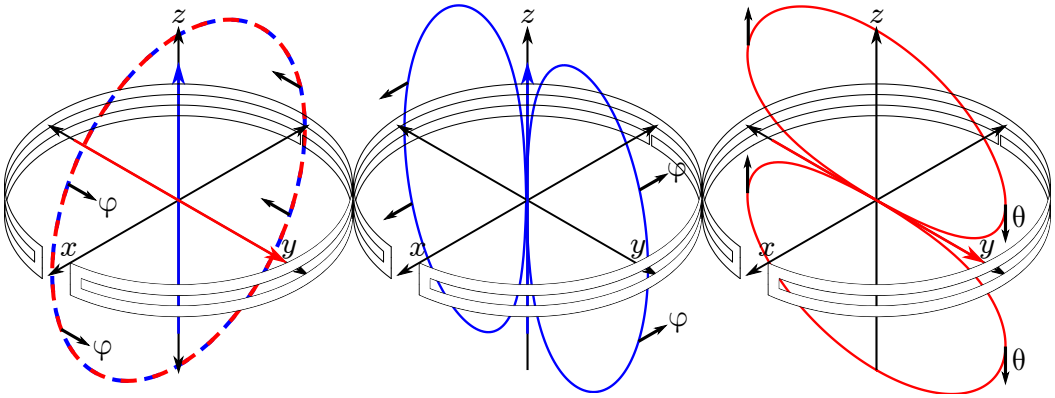

(a) (b) (c)

Figure 3.4: Electric and magnetic dipole modes of the FSRR demonstrated by decomposing directivity into θ and φ components. In the $\varphi = 0°$ plane (a) both modes radiate with φ polarisation. In the $\varphi = 90°$ plane the magnetic dipole radiates with φ polarisation (b) and the electric dipole with θ polarisation (c).

the $\varphi = 90°$ cut for (b) and (c). The blue trace shows magnetic dipole contributions and the red trace shows electric dipole contributions. In the $\varphi = 0°$ plane, the fields from the electric and magnetic dipoles are both φ-directed and hence combine to form the circular trace. In the $\varphi = 90°$ plane, the dipole components are orthogonal to each other; the blue magnetic dipole mode is

φ-directed and the red electric dipole mode is θ-directed.

The radiation is a maximum in the $\varphi = 0°$ plane, due to the combined contribution of the φ-directed dipole modes. The lack of deep nulls in the FSRR antenna's pattern is demonstrated by Figures 3.4(b) and (c). In this plane, the direction in which the magnetic dipole mode's field is a minimum is the same direction in which the electric dipole mode's field is a maximum, and vice-versa.

The fact that the fields in the plane of maximum directivity are φ-directed suggests that the receiving antenna should be oriented in the same direction, depending on how the transmitting antenna is mounted on the rhinoceros's leg.

3.3 Tuning Parameters

The electrical size of the model simulated in Section 3.4.1 is $ka = 0.49$ which is below our project's upper ka limit of 0.57. However, the FSRR antenna's circular shape prevents it from fitting inside the rectangular enclosure. The simulated model may be seen above the enclosure in Figure 3.5. The antenna's diameter is 107.39 mm which is larger than the enclosure's 65 mm width. Optimisation of the antenna in Section 3.4.1 will lower the diameter, but not to a dimension that is necessary for the antenna to fit inside.

The antenna's shape will therefore need to be adapted to fit inside the enclosure. This process will be detailed in Chapter 4. The adaptation process will lower the reflection efficiency of the FSRR antenna at our system's operating frequency. To increase the efficiency the FSRR antenna's tuning parameters may be adjusted to change the antenna's input impedance to match the transmission line.

Furthermore, the antenna will operate inside a plastic enclosure, in close proximity to a rhinoceros's body. The presence of these dielectric bodies in the near-field of the antenna will also affect the antenna's impedance. Once again, the tuning parameters may be adjusted to reduce these effects.

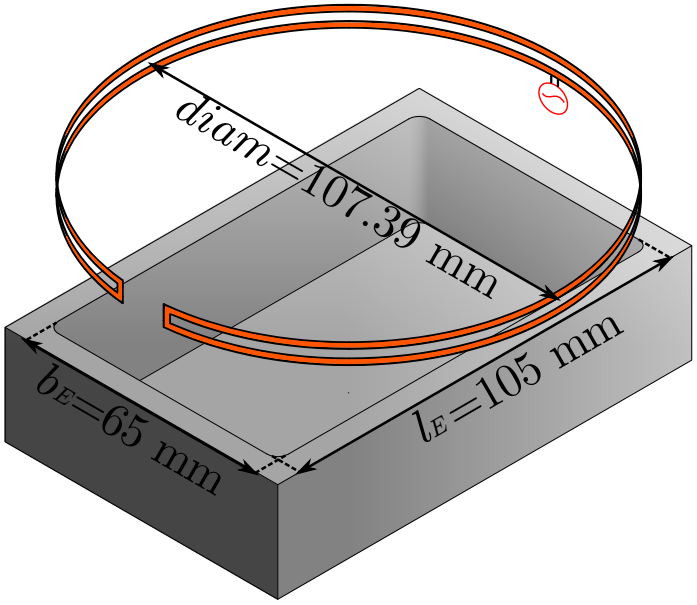

Figure 3.5: The tag enclosure with the prototype model superimposed. With its current shape, the antenna is too large to fit inside the enclosure.

There are two parameters that determine the input impedance of the FSRR antenna. The gap length gl may be adjusted to tune f_{res} and the conductor width ratio w_2/w_1 may be adjusted to tune Z_A.

It would be desirable to know the effectiveness of these tuning methods to see to what extent they can be utilised during the adaptation process in Chapter 4. To illustrate this, two experiments are performed using the models from section 3.2.

3.3.1 Effect of the Gap Length

The FSRR antenna reported by Kim and Nam, described in Section 2.6, uses an interdigital capacitor at the conductor's ends to tune f_{res} [39]. A representation of the interdigital capacitor may be seen at the top in Figure 3.6. It is created by cutting the ends of the conductors into serrated "teeth", whose dimensions are controlled to achieve a desired capacitance between them. By increasing the capacitance, the f_{res} is decreased. To reduce the complexity, the FSRR antenna models simulated in this project remove the interdigital capacitor. To control the capacitance between the conductor ends the gap

length gl is adjusted.

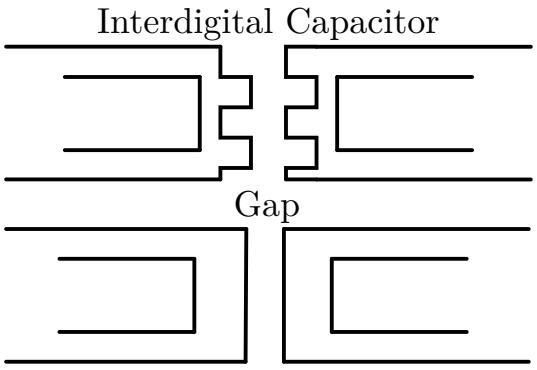

Figure 3.6: At the top is the interdigital capacitor between the ends of the FSRR. At the bottom the interdigital capacitor is removed.

To assess the extent to which the gap length can control f_{res}, an experiment was performed in which gl was varied. For the experiment, gl was varied between 1 mm and 25 mm with a step size of 0.05 mm. This corresponds to wavelengths between 0.001λ and 0.036λ, with a step size of 0.001λ. The total length dl, the widths w_1, w_2 and the spacing s were kept constant throughout the experiment. This meant that the diameter of the antenna would decrease with decreasing gl. The resulting resonant frequency for the various gap lengths is plotted in Figure 3.7.

The resonant frequency of the FSRR antenna simulated in Section 3.2 is indicated by the arrow on the plot in the figure. Its gap length is $gl = 0.019\lambda$. To the left, as the gap length decreases, the resonant frequency decreases rapidly, reaching a minimum value of 413 MHz. The figure also shows that the rate at which f_{res} increases decreases with the gap length gl. At the maximum gap length of $gl = 0.036\lambda$ the $f_{res} = 438$ MHz.

Varying the gap length is therefore more effective for lowering f_{res}, as opposed to raising it. However, the achieved decrease in f_{res} is only 4.6%, which indicates that variation of the gap length can be used to make fine adjustments to the resonant frequency.

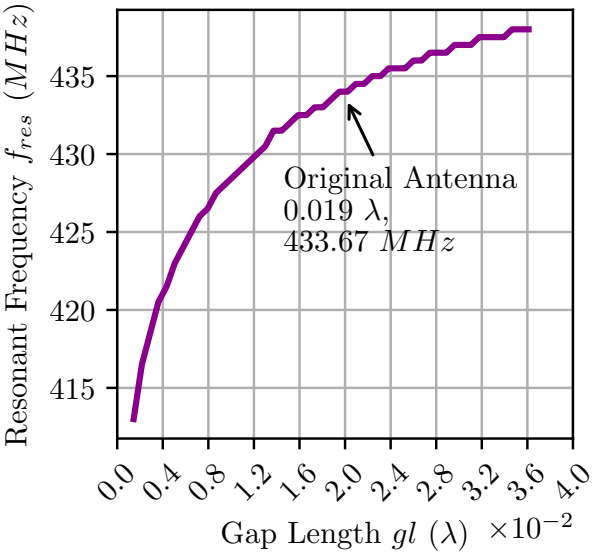

Figure 3.7: Resonant frequency f_{res} for different gl values of the FSRR antenna. The f_{res} decreases with decreasing gl.

One undesirable effect of a decrease in gl is the associated reduced R_{rad}, which decreases from $R_{rad} = 47.80\ \Omega$ for the original model to $R_{rad} = 34.54\ \Omega$ for the $gl = 0.001\lambda$ model. This is presumed to be due to the decrease in ka that accompanies the decreased R_{rad}. As the following experiment will show, this reduced R_{rad} can be recovered by increasing the conductor ratios.

3.3.2 Effect of the conductor ratio

In Section 3.2 it was shown that the FSRR resonates with an R_{rad} close to 50 Ω. The high R_{rad} is due to the magnetically coupled parallel conductors. In Section 2.4.3 it was mentioned that the R_{rad} of the folded dipole was proportional to the ratio w_2/w_1. Kim indicates in [39] that the FSRR antenna's R_{rad} may be controlled in the same manner.

An experiment was conducted to determine the extent to which increasing the w_2/w_1 ratio increases R_{rad}, for both the folded dipole and the FSRR. The combined width $w_1 + w_2$ of both conductors remained constant while varying w_2/w_1. This meant that an increase in w_2/w_1 would increase w_2 and decrease w_1. The simulation models of the previous experiment were used again, but the metal was changed from PEC to lossy copper. This was done to account

for the increased conductor losses that were expected to result from a decrease in the lower conductor's width w_1, with an increased w_2/w_1 ratio. Due to the marginal increase in simulation time that the copper's inclusion caused, it was decided to incorporate it into all subsequent simulations to improve their accuracy.

For both antennas the conductor ratios w_2/w_1 were varied between 1 and 15 in steps of 0.5.

The resulting input resistance R_{in} values are plotted against the w_2/w_1 values in Figure 3.8. The green trace shows the R_{in} of the folded dipole antenna and the black trace the R_{in} of the FSRR antenna. R_{in} increases for both antennas as w_2/w_1 increases, as expected. The R_{in} of the FSRR increases from 48.90 Ω when $w_2/w_1 = 1$ to 136.77 Ω when $w_2/w_1 = 15$, representing a factor 3.7 increase, where the folded dipole increases by a factor of 3.37, from 283.935 Ω to 956.456 Ω.

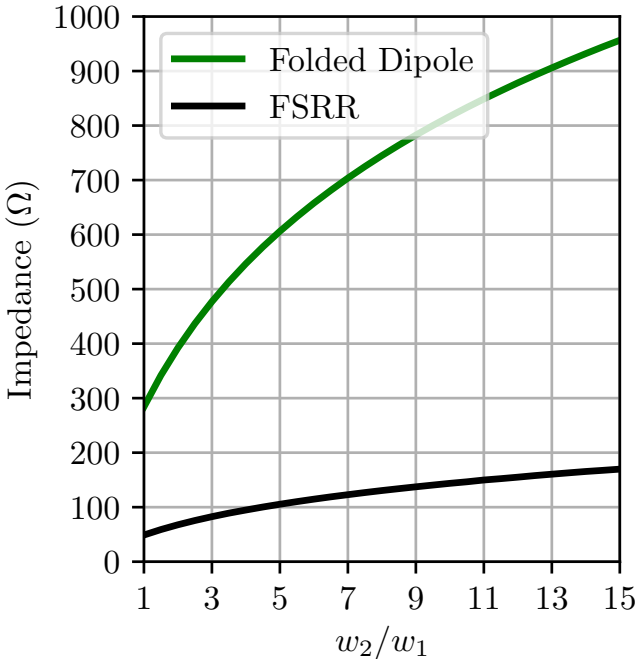

Figure 3.8: The input impedance R_{in} plotted against the conductor width ratio w_2/w_1 of a simulated FSRR and folded dipole antenna. By increasing w_2/w_1 above unity R_{in} may be increased.

Both gradients decrease with increasing w_2/w_1 and the factor by which the two impedances increase for both antennas is similar. The efficiency values were not significantly affected, contrary to what was anticipated.

The achievable increase in R_{in} is substantial and will prove useful when adapting the antenna's shape to fit inside the enclosure.

3.4 Design, Optimisation and Construction

With the operation of the FSRR understood, the simulated FSRR antenna from Section 3.2 is optimised, simulated and constructed.

3.4.1 Design and Optimisation

Prior to optimisation, an FR-4 substrate was added to the simulation model. This is the blue layer shown in Figure 3.9, which is a representation of the optimised model. The substrate was 0.2 mm thick with a permittivity of $\epsilon_r = 4.6$ and a loss tangent of $\tan\sigma = 0.017$. Compared to the literature where $\epsilon_r = 2.9$ and $\tan\sigma = 0.002$, the FR4 losses and permittivity values are higher. The effect of the FR-4 substrate is to slightly lower f_{res} from 433.69 MHz to 427.00 MHz. Due to the thin substrate, the radiation efficiency was not significantly affected.

The model was then optimised to most closely match a 50 Ω input impedance. A detailed understanding of the optimisation algorithm is beyond the scope of this thesis, so it was opted to let FEKO decide the method automatically. This led to the Nelder-Mead search algorithm being chosen. The resulting optimised dimensions are given in table 3.1. During the optimisation, the w_2/w_1 ratio was kept at unity to maintain the model's simplicity. The optimised values are similar to those of the base model because this was already well-matched.

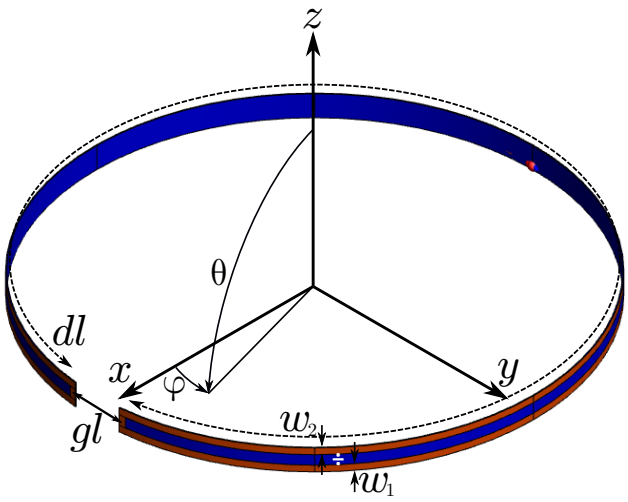

Figure 3.9: Optimised model of the simulated FSRR antenna. Thin FR-4 substrate was added to allow flexibility when manufacturing.

Table 3.1: The optimised dimensions of the simulated FSRR antenna.

Parameter (mm)	**Optimised Model**
dl	315.80
gl	10.40
s	3.13
w_1	1.38
w_2	1.38

3.4.2 Construction

The prototype was then constructed in the Stellenbosch Engineering Faculty workshop. The main radiator was created using a standard PCB drilling machine and is shown in Figure 3.10.

3.4.2.1 The Sleeve Balun

Because the FSRR antenna is a balanced structure, a balun was required to feed it to a coaxial connector. The sleeve balun was chosen due to its design simplicity and good performance. The designed balun is shown in Figure 3.11(a). It comprises an approximately quarter-wavelength long copper tube, with the end furthest from the radiator short-circuited to the coaxial shield. At a distance of one quarter-wavelength from the short-circuited end, any current flowing along the outside of the shield will experience an infinite impedance.

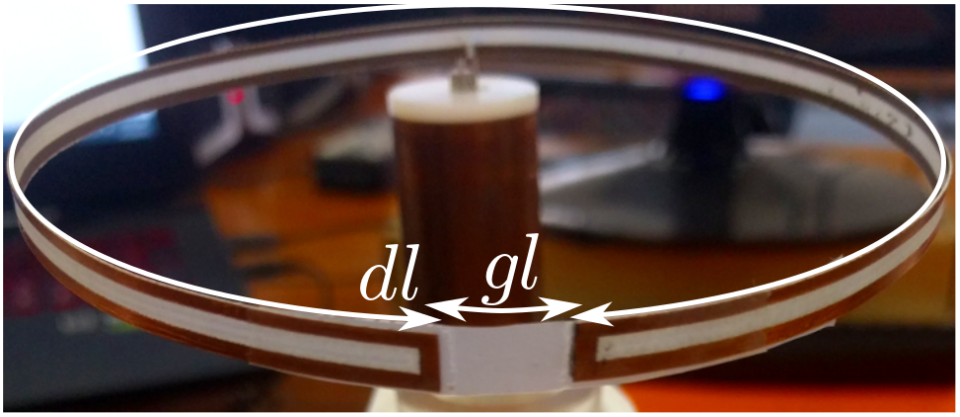

Figure 3.10: The constructed FSRR antenna.

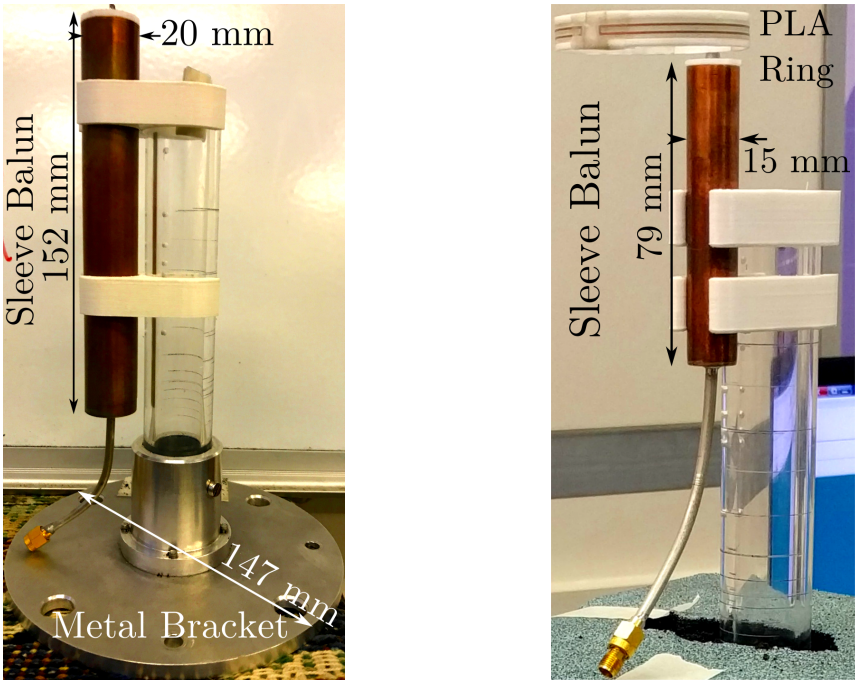

(a) (b)

Figure 3.11: (a) The attached sleeve balun and metal plate. (b) The half-size scaled FSRR antenna.

Thus, return currents are restricted to flow inside the coaxial connector only [40].

The sleeve balun was designed according to [41]. The paper gives the required copper tube length for the sleeve balun to provide maximum choking capability, given the diameters of the copper tube and the coaxial cable. For

this project, the copper tube diameter used was 20 mm and the coaxial cable diameter used was 3.7 mm. This led to a required tube length of 152 mm.

This sleeve balun is too long to fit inside the 105 $mm \times 65\ mm \times 25\ mm$ enclosure, even without the antenna attached. In Chapter 4 a smaller balun is investigated.

3.4.2.2 The Metal Plate

Figure 3.11(a) also shows the metal bracket that was used to mount the antenna in the anechoic chamber, for pattern measurements. The diameter of the bracket is 147 mm. It was designed to mount heavier antennas which is why it is constructed from metal. Unfortunately, the metal caused unwanted scattering, the effects of which will be observed in Section 3.5.

3.4.2.3 The Scaled Model

The lowest frequency at which measurements can be made in the anechoic chamber at Stellenbosch University is 750 MHz. Since this is almost double the operating frequency of our system, the frequency scaling theorem was used to scale the constructed FSRR antenna by a half, theoretically doubling the operating frequency to $f_{res} = 866\ MHz$. The constructed model is shown in Figure 3.11(b), attached to the scaled balun. This model was used for radiation pattern measurements.

The balun dimensions were chosen by following the same process as the original model and they are shown in Figure 3.11(b).

The dielectric thickness could not be scaled as it was the thinnest substrate available. However, simulations had revealed that adding the FR-4 substrate to the simulated base model had a negligible effect on the pattern. It was therefore presumed that keeping the same thickness would not invalidate the scaling results.

A polylactic acid (PLA) plastic ring was also used to keep the antenna's shape circular, in the hope of better preserving the shape of the radiation pattern. The ring was kept very thin, approximately 0.5 mm, to reduce its effect on the radiation pattern. It was later realised, however, that the ring affected the antenna's resonant frequency f_{res} by reducing it from 832 MHz to 816.7 MHz. The antenna was measured at this frequency to compare radiation patterns.

3.5 Measurements and Results

For this project reflection coefficient measurements were made using the Rhodes & Schwartz ZVB 8 vector network analyser (VNA), with the scaled antenna. Pattern measurements were conducted inside an anechoic chamber using a spherical near-field scanner (SNF) and an Agilent PNA-X 5242A VNA. In the chamber a RGP-10 horn antenna was used as the probe. It was fixed in place during the scan while the antenna under test (AUT) (the scaled FSRR antenna) was rotated. The setup of the two antennas inside the chamber is shown in Figure 3.12. The probe antenna was placed 768 mm from the AUT. This distance is well within the far-field, which starts at a radius of 31.21 mm from the AUT.

When the AUT rotated in the θ plane between $\theta = 90°$ and $\theta = 270°$ it's own supporting arm blocked it from the probe's line of sight. Therefore, all pattern traces should be ignored between these θ values.

The analysis first considers the electrical size of the models. The resulting impedance values are then analysed and converted to reflection efficiency values. The directivity polar plots are then examined. The radiation efficiency e_{rad} is subsequently combined with the reflection efficiency e_{ref} values to determine total efficiency e_{tot}. This is applied to the maximum and minimum directivity values to obtain the corresponding realised gain values $G_{rl,max/min}$.

The simulated electrical size of the optimised and measured model was $ka = 0.47$ and $ka = 0.48$, respectively. The difference is due to a slight shift in f_{res} between the two and it is thought to be a result of the constructed

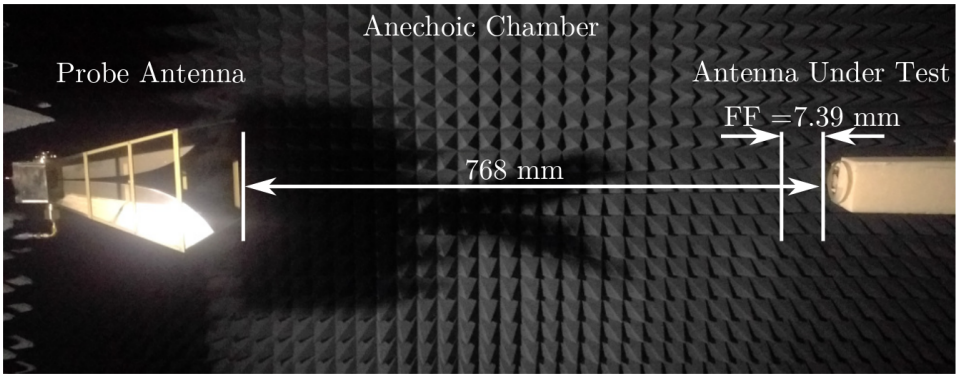

Figure 3.12: The anechoic chamber setup for the prototype FSRR directivity measurement.

antenna's gap length gl differing slightly to the simulation antenna's gl. The values of ka are both below the upper limit of the required relative size of 0.57.

3.5.1 Impedance

The reflection coefficient Γ plot is shown in Figure 3.13. The solid red trace and the dashed red trace represent the response of the simulated model and the constructed model, respectively. The simulated model's lowest reflection coefficient value is at $f_{res} = 435.5\ MHz$ with a value of $\Gamma = -26.21\ dB$ which corresponds to $e_{ref} = 99.76\%$. For the measured model the lowest reflection coefficient value is at $f_{res} = 436.5\ MHz$ with $\Gamma = -17.14\ dB$ which corresponds to $e_{ref} = 98.2\%$. The measured value satisfies the design requirements and the traces match closely.

3.5.2 Radiation

The directivity polar plots for the simulated and measured model at their resonant frequencies are shown in Figure 3.14(a), (b) and (c). For each plot the simulated free space (no mounting bracket) model is given by the solid light blue line. The maximum directivity is 1.25 dBi and occurs in the $\varphi = 0°$ plane in (a), toward $\theta = 90°$. The minimum directivity is $-1.85\ dBi$ in the $\varphi = 90°$ plane in (b), also toward $\theta = 90°$. The relatively high minimum directivity highlights the quasi-isotropic characteristic of the pattern.

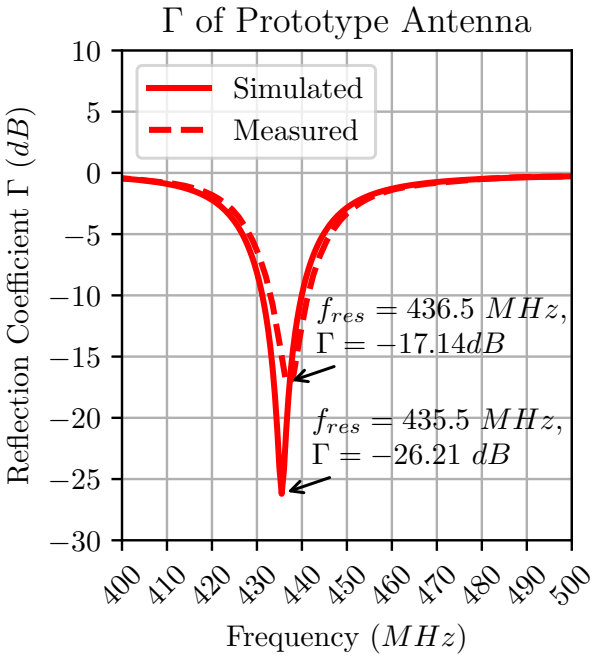

Figure 3.13: Reflection coefficients of the simulated prototype FSRR antenna versus the constructed prototype.

The dark blue dashed trace indicates the measured pattern. It is postulated that the scattering from the bracket distorts the radiation pattern. The effect is to create high directivity lobes away from the horizon, and to create a trough of low directivity close to $\theta = 0°$. The effects are most noticeable in Figure 3.14(a) in which the maximum directivity is now 3.99 dBi toward $\theta = 298°$ and the minimum directivity is -3.26 dBi toward $\theta = 6°$.

The overall maximum directivity shifts to the $\varphi = -4°$ plane with a value of 4.09 dBi toward $\theta = 296°$. Compared to the simulated model, the difference between the overall maximum and minimum directivity values increases from 3.10 dBi to 7.35 dBi. Clearly, the uniformity of the quasi-isotropic pattern has been reduced.

To determine whether the bracket is the cause of the distortion, it is added to the free space simulated model, along with the plastic ring. This result is indicated by the green dash-dotted trace which more noticeably aligns with the measured trace. This is quantified by the decreased average difference in directivity between the measured and simulated model. The difference be-

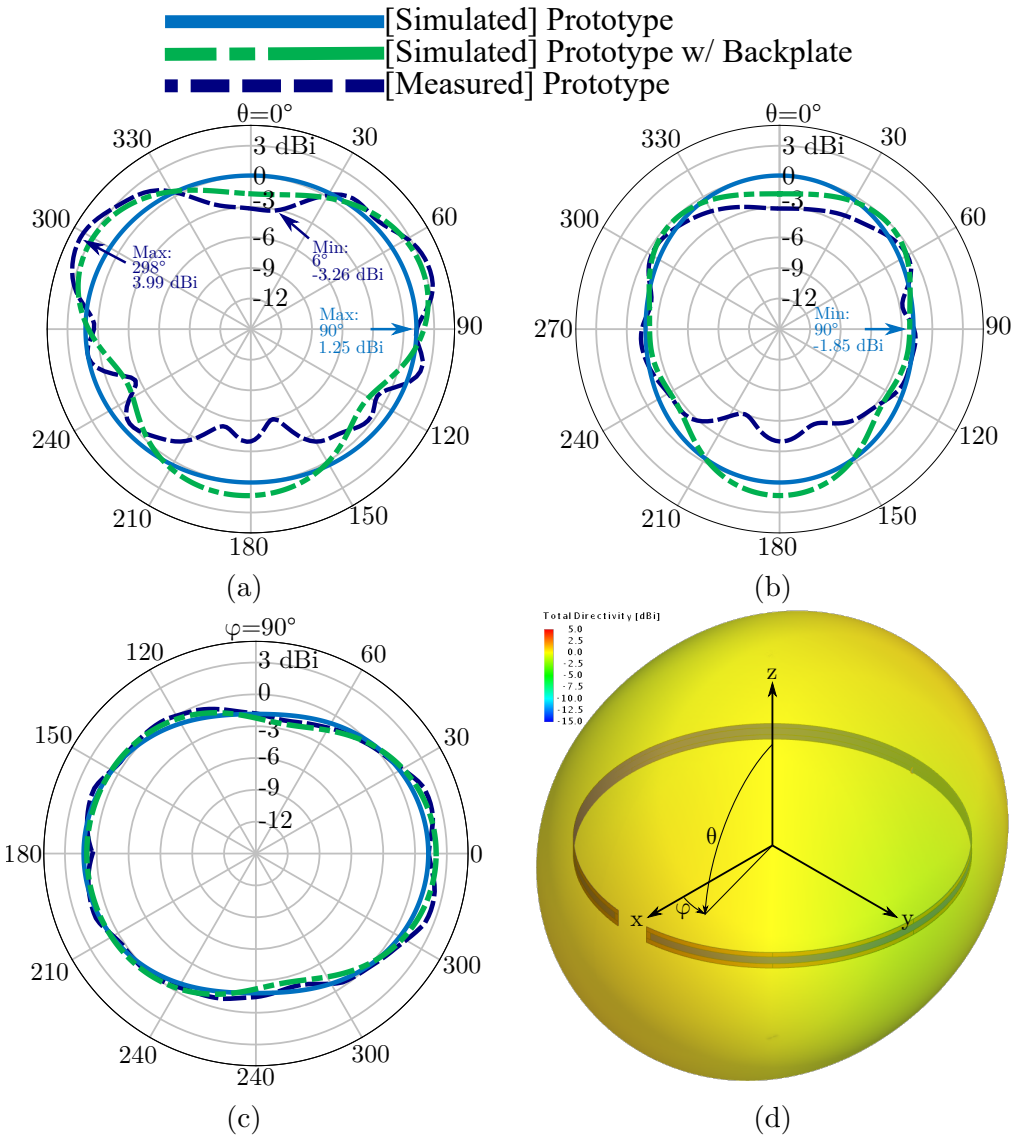

Figure 3.14: Far-field total directivity plots of the measured and simulated circular prototype FSRR antenna. (a)-(c) The far-field polar plots of the measured and simulated antenna, simulations with and without a bracket, for (a) the $\varphi = 0^\circ$ cut, (b) the $\varphi = 90^\circ$ cut and (c) the $\theta = 90^\circ$ cut. (d) The simulated 3-dimensional plot of the model with no bracket, whose orientation may be used as a reference for both simulated and measured models.

tween simulated and measured directivities was taken over each point of the far-field between $270^\circ \leq \theta \leq 90^\circ$ and averaged, for both the free-space and plate simulation. The average difference between simulated and measured directivity decreases from $-3.81\ dB$ to $-6.24\ dB$ when the plate and plastic ring are added.

This indicates that the initial simulated model should radiate similarly to an equivalent bracket-less measured model, with an average directivity error of approximately $-6.24\,dB$. The initial simulated model has thus been validated.

The radiation efficiency e_{rad} was not measured for this model and hence the simulated e_{rad} will be used to calculate the total efficiencies e_{tot} of both the simulated and constructed models, according to Equation 2.11. Application of this equation, using the simulated $e_{rad} = 95.76\%$, results in a simulated e_{tot} of 95.53% and a measured e_{tot} of 94.04%.

3.5.3 Comparison

The performance of our measured prototype FSRR antenna will now be compared to the measured FSRR design reported by Kim and Nam [39]. The electrical size ka, total efficiency e_{tot} and minimum and maximum realised gain values $G_{rl,max}$ and $G_{rl,min}$ of the two models are given in Table 3.2. Each value is from the respective measured model, with the exception of the total efficiency of our prototype which was calculated using the simulated radiation resistance. It should be remembered that the realised gain is related to the directivity by $G_{rl}(\theta, \varphi) = e_{tot} D(\theta, \varphi)$.

The smaller electrical size reported by Kim and Nam is presumably due to the use of an interdigital capacitor between the conductor ends which could provide higher system capacitance. However, the use of the gap for the optimised circular model reduces design and construction complexity. The total efficiency achieved by our prototype model is high. The total efficiency of the author's model is higher, due to a combination of lower losses in the dielectric and slightly better matching. The matching of our antenna will be improved in Chapter 4.

The maximum realised gain of our prototype model is 1.61 dB higher than the model reported by Kim and Nam. The minimum realised gain is 0.97 dB lower. These large disparities are most likely a result of the non-uniformity of

Table 3.2: The measured parameters of our prototype FSRR antenna versus those found for a FSRR design in the literature [39].

Parameters	**Our Prototype**	**Prototype by Kim [39]**
ka	0.48	0.41
e_{tot} (%)	94.04	91.32
$G_{rl,max}$ (dBi)	3.72	2.11
$G_{rl,min}$ (dBi)	-3.53	-3.08

our prototype's measured pattern.

The simulated realised gain values of our prototype and of the model designed by Kim and Nam will be compared instead, in order to remove the undesirable effects of the bracket. The simulated maximum and minimum realised gains of our prototype model are $G_{rl,max} = 1.06\ dBi$ and $G_{rl,min} = -2.05\ dBi$, respectively. The simulated maximum and minimum realised gains of Kim and Nam's model are $G_{rl,max} = 1.33\ dBi$ and $G_{rl,min} = -1.01\ dBi$, respectively.

The difference in maximum simulated gain of 0.26 dBi between the two models is significantly lower than the difference between the maximum measured values. The difference in minimum simulated realised gain is increased slightly, but only by 0.07 dB. The two model's realised gains are similar, although the minimum realised gain of the model designed by Kim and Nam is greater than our prototype's realised gain by 1.04 dBi. Here, both maximum realised gain values satisfy the $G_{rl,max}$ requirements of being greater than 0 dBi. However, they do not reach the performance of a half-wave dipole, $G_{rl,max} = 1.95\ dBi$, which is preferred. Given that the $G_{rl,min}$ of the FSRR antenna is much higher than the $G_{rl,min}$ of a dipole, the lower maximum realised gain of the FSRR antenna is deemed acceptable.

Therefore, we can conclude that a prototype FSRR antenna was successfully implemented on affordable FR-4 substrate while satisfying the design requirements. The results of the simulated and measured models show satisfactory agreement in order to validate the FEKO model.

3.6 Summary and Conclusion

A simulation model of a FSRR antenna, designed to operate at 433 MHz, was examined and its similarities and differences to a more simple folded dipole antenna were investigated. The folded conductors in both antennas were found to raise the input impedance to a similar extent. The tuning parameters were successfully investigated and their effectiveness toward miniaturisation and dielectric disturbances was noted. Subsequently, a simple prototype model was optimised and constructed. Good agreement between the measured and the simulated characteristics of this antenna was demonstrated. Our FSRR prototype was also found to behave similarly to a comparable design reported in the literature, and satisfied the design requirements even though it was manufactured on a cheaper substrate. Although our prototype does not fit inside the enclosure in its current form, it will be used as a benchmark to compare to an adapted FSRR antenna in the next chapter.

Chapter 4

Adaptation of the FSRR Antenna

4.1 Introduction

The initial prototype satisfied the design requirements, despite being manufactured on affordable but lossy FR-4 substrate. However, both its diameter and the attached sleeve balun were too large to fit inside the rectangular enclosure.

This chapter primarily details the process of adapting the first prototype FSRR antenna to fit inside the specified enclosure by changing its shape from circular to rectangular. The antenna is also reduced to a 2-dimensional planar form, which is suitable for printing on rigid substrate, and allows a small surface mount (SMT) balun to be soldered directly onto it. A representation of the final adapted configuration is shown in Figure 4.1.

The adapted rectangular prototype antenna will be constructed and compared to the simulated model for validation. The adapted rectangular prototype will then be compared to the first prototype to assess whether it maintains the characteristic FSRR behaviour.

Finally, we will examine the impedance response of the adapted rectangular prototype antenna when it is placed directly inside the enclosure and in close proximity to a human arm. This will give an approximation of its behaviour in close proximity to a rhinoceros.

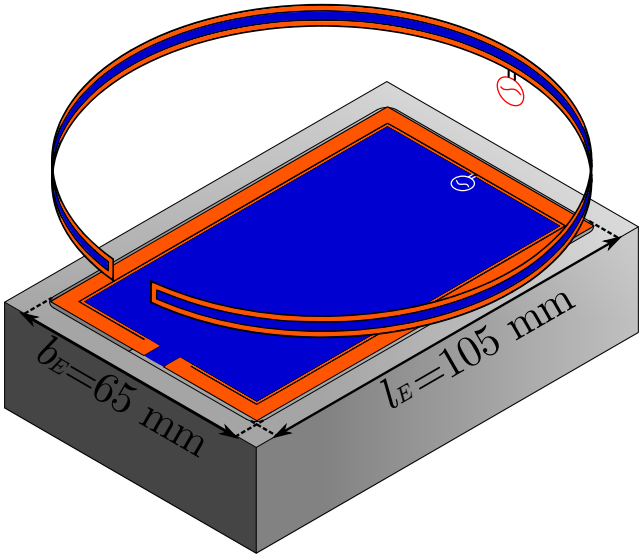

Figure 4.1: Model of the final configuration adapted to fit inside the enclosure.

4.2 Planar Transformation

The first transformation is the reduction of the 3-dimensional prototype model to a 2-dimensional planar form. To reduce simulation run-times, the substrate was removed for the initial transformations. The effect of the substrate is then examined later in Section 4.4. A representation of this transform is shown in Figure 4.2(a). It can be seen that the length *dl* measured along the middle of the two conductors of the transformed model is kept equal to the corresponding length of the first prototype.

Simulations show that the planar transformation has a negligible effect on the performance of the FSRR antenna. The reflection coefficients of the first and the transformed model are plotted in Figure 4.3. It is evident that the traces align closely. Note that the optimised model's substrate has been removed in these simulations, which is why the resonant frequency is now 444 MHz.

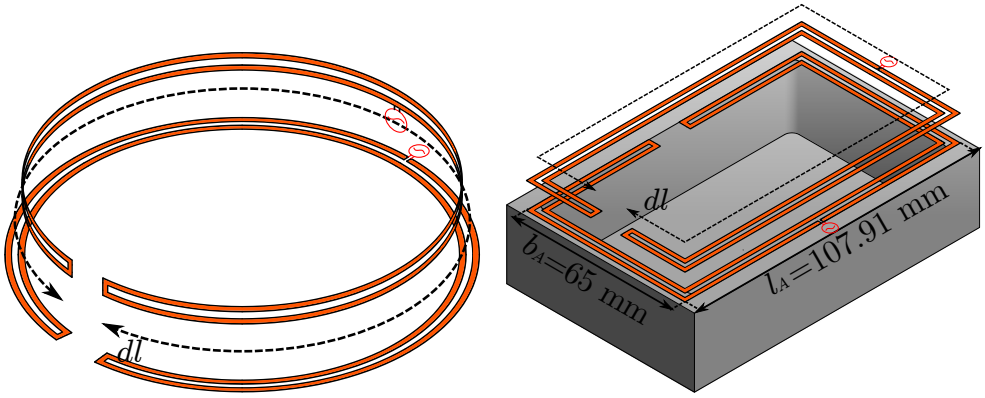

(a) (b)

Figure 4.2: Model of the first prototype transformed to a planar configuration in (a). This planar configuration is transformed to two rectangular configurations in (b).

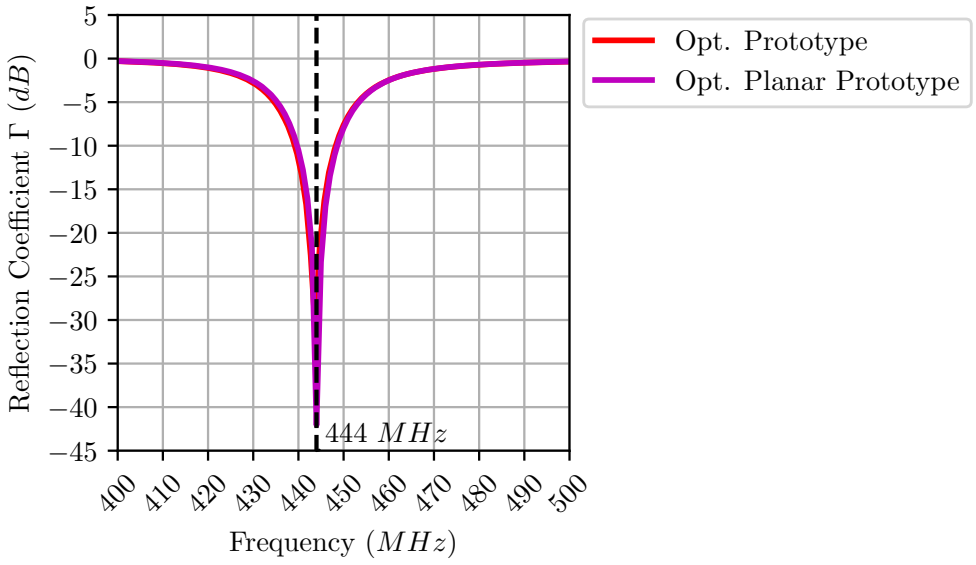

Figure 4.3: Reflection coefficient of the optimised prototype and the transformed planar model, both shown in Figure 4.2(a). The substrate has not been taken into account when computing these results.

4.3 Rectangle Transformation

The planar model is now transformed from a circular to a rectangular shape and the resulting change in performance examined. The total length through the conductor centres *dl* is kept constant between transformations. The transform is shown in Figure 4.2(b). Two variations of the rectangular configura-

tions were considered. The first places the feed and gap along the breadth of the antenna, as shown by the top model in Figure 4.2(b). This model will be referred to as the first rectangular configuration. The second variation places the feed and gap along the length of the antenna, as shown by the lower model in Figure 4.2(b). This model will be referred to as the second rectangular configuration.

The breadth of both configurations corresponds to the inner breadth of the enclosure, as seen in Figure 4.2(b), so $b_A = b_E = 65\ mm$. This leads to an antenna length of $l_A = 107.91\ mm$ which is longer than the enclosure inner length l_E. Steps will be taken in later sections to reduce the antenna size.

The reflection coefficients are examined first and plotted in Figure 4.5. We see that the resonant frequency f_{res} of both configurations increases substantially compared to the planar circular prototype, with the second rectangular configuration exhibiting $f_{res} = 478\ MHz$. This may partly be explained by the corners of the rectangular configurations. Current nulls occur on the corners and they are expected to shorten the current path along the conductors. The current density on the corners of the first rectangular configuration is depicted in Figure 4.4. The green and blue areas indicate segments of low current density. The orange and red areas indicated segments of high current density. The red arrows represent the current direction. The low densities of current can clearly be seen, especially near the outer corners of each conductor. It is suspected that the contribution of the current nulls to the raised frequency is small. It is therefore recommended to investigate additional reasons as to why this increased f_{res} occurs.

The Γ of the first rectangular configuration is a relatively high $-13.25\ dB$ at $f_{res} = 471\ MHz$, which corresponds to $e_{ref} = 91.19\%$. This is a result of the decrease in input resistance to $R_{in} = 32.14$, from 50.21 Ω of the planar circular model. Conversely, R_{in} for the second rectangular configuration is higher than that of the optimised planar model. It is presumed that this behaviour is related to the feed and gap placement. From section 3.2 the even mode current maximums occur along the feed and the gap. It can be seen in Figure 4.2(b) that the straight conductor segments along which these current

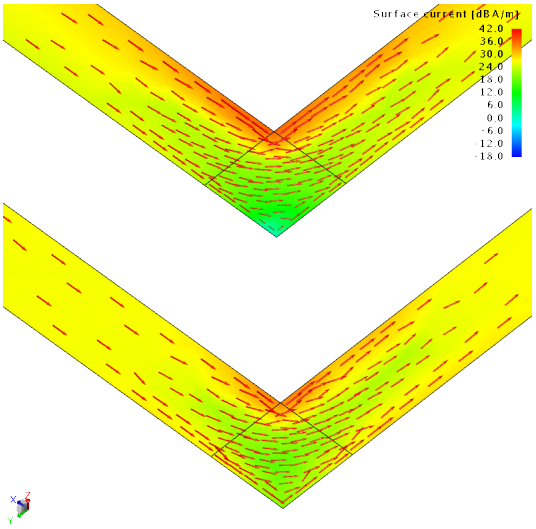

Figure 4.4: Current density of the first rectangular configuration, along one of its corners.

maximums occur will behave approximately as dipoles, with the current maximums acting as the centre-fed sources. Because the second configuration's feed and gap are placed on longer segments the radiation resistance for this configuration is higher.

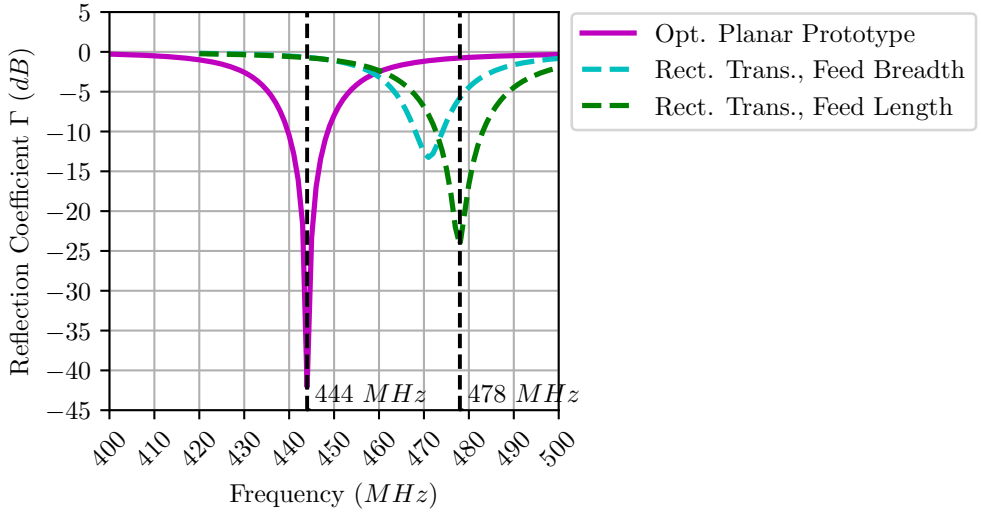

Figure 4.5: Reflection coefficients for the circular optimised planar FSRR and the two rectangular transformations. The rectangular configurations both correspond to the shape of the enclosure.

The increased radiation along the second configuration's side length also implies a stronger electric dipole. In Figure 3.4(c) of Section 3.2, the electric dipole mode was observable in the $\varphi = 90°$ plane with maximums toward $\theta = 0°$ and $\theta = 180°$. Stronger radiation from the electric dipole mode would increase these maximums. This behaviour is displayed by the second rectangular configuration in Figure 4.6(a). The figure depicts the $\varphi = 90°$ polar plot cut and the directivity of the second rectangular configuration is indicated by the dashed green trace. Of the three configurations, we see that the directivity towards $\theta = 0°$ and $\theta = 180°$ of the second rectangular configuration is the greatest. The directivity in these directions is $D = 0.76\ dBi$. The second rectangular configuration's minimum directivity is also the lowest, with $D = -3.74\ dBi$ toward $\theta = 270°$, compared to the minimum directivity of the original planar circular configuration of $D = -1.45\ dBi$ toward $\theta = 90°$. This suggests that the effect of the magnetic dipole mode has decreased for the second rectangular configuration. This may be due to low currents along the conductor segments that do not contain the feed or the gap.

The total efficiencies are applied to the maximum and minimum directivity values and are summarised, together with the resonant frequencies, in Table 4.1. Changing from a circular to a rectangular shape increases the resonant frequency in both cases. The maximum realised gain of the rectangular configuration is 0.83 dBi lower than the that of the second. However, the second configuration's minimum realised gain is even lower, by 2.27 dBi. This difference cannot be sufficiently recovered through tuning since the reflection efficiency is already close to 100% for the second rectangular configuration. On the other hand, the first rectangular configuration has more tuning potential. Therefore, the first configuration, with feed along the antenna's breadth is chosen.

4.4 Further Miniaturisation and Substrate Addition

The antenna's shape now matches the enclosure's, but its length is too long by 2.91 mm. Physically, the antenna length and breadth dimensions should be slightly less than the enclosure's inner dimensions so that it can be in-

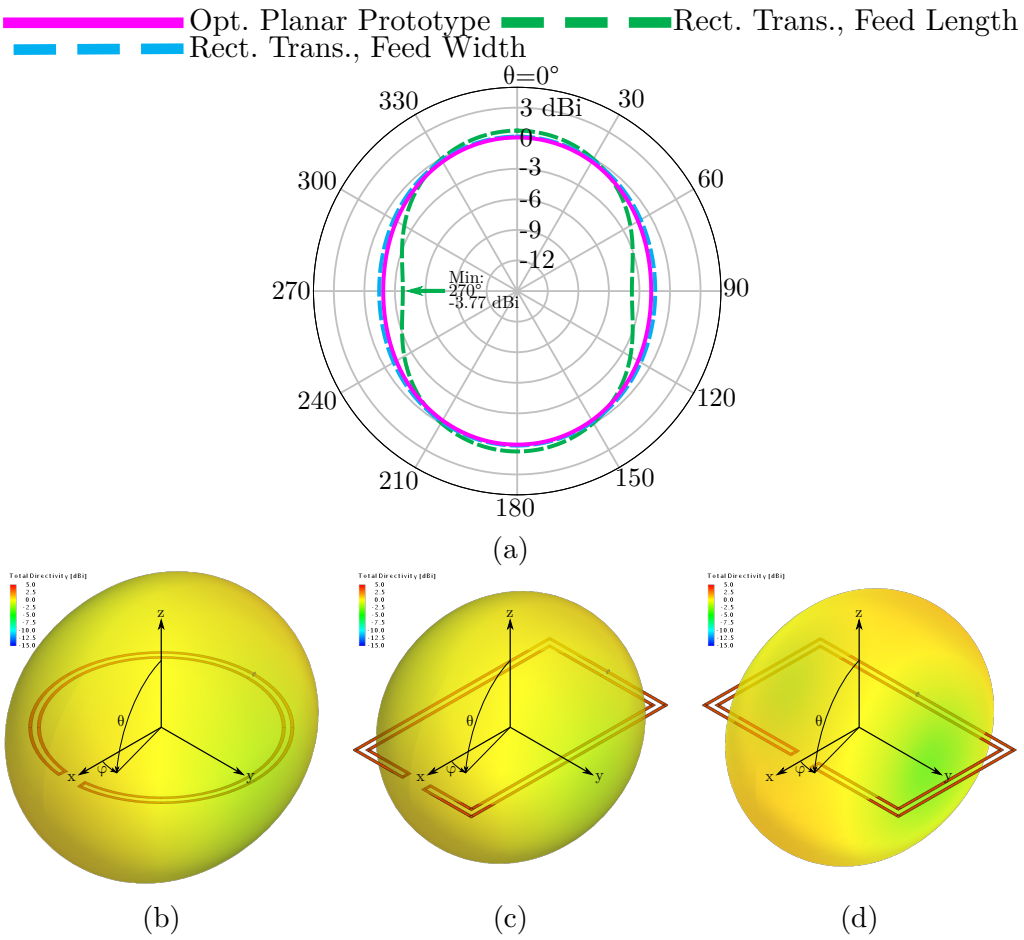

Figure 4.6: Far-field total directivity plots of the optimised circular planar FSRR antenna, and two rectangular transformations. In (a) the $\varphi = 90°$ polar plot. In (b)-(d) the 3-dimensional directivity plots for each configuration.

Table 4.1: The parameters of the simulated circular planar FSRR antenna compared to two variations of a rectangular planar FSRR antenna.

Parameters	**Circular Planar**	**Rectangular, Feed Breadth**	**Rectangular, Feed Length**
f_{res} (MHz)	433	471	478
e_{tot} $(\%)$	97.02	90.69	96.89
$G_{rl,max}$ (dBi)	1.11	0.52	1.35
$G_{rl,min}$ (dBi)	-2.03	-1.85	-4.12

serted easily. The rectangular model's length and breadth are reduced to $l_A = 103.5\ mm$, $b_A = 63.5\ mm$ to satisfy this and the effects are examined.

A substrate must also be added to manufacture the antenna. It is desirable

to keep the antenna rigid, so a thicker substrate was chosen. The available rigid FR-4 substrate was 1.57 mm thick, so this was applied to the rectangular model. The transformation of the first rectangular configuration to the miniaturised configuration with substrate added is shown in Figure 4.7.

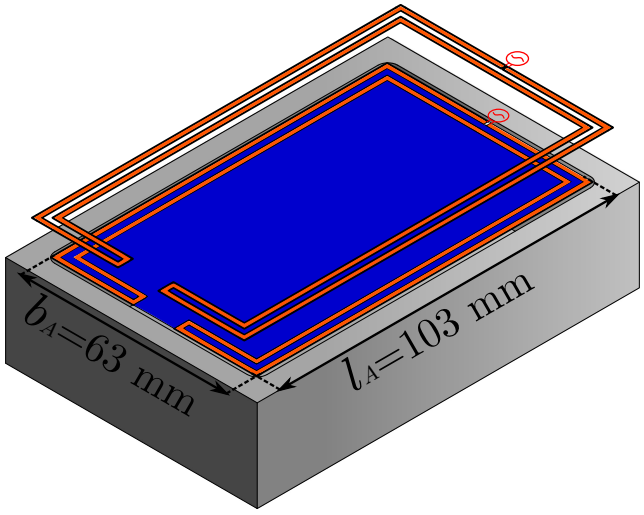

Figure 4.7: Model of the first rectangular configuration transformed to a smaller model with added substrate. The model now comfortably fits inside the enclosure.

In comparison to the optimised circular planar prototype, the rectangular prototype includes a larger volume of substrate. It is expected that the thicker substrate will strengthen the electric field across the gap between the ends of the conductor, causing a decrease in f_{res} compared to the thinner substrate. The effect of adding this substrate to the miniaturised configuration will also be examined. The 0.2 mm thick substrate used for the planar circular configuration as well as the 1.57 mm thick substrate used for the rectangular configuration will be simulated. During these comparisons it was seen that the directivity was not significantly affected and hence only the efficiencies will be considered.

The reflection coefficients for each configuration are plotted in Figure 4.8. By decreasing the dimensions of the rectangular FSRR antenna, the resonant frequency increases from $f_{res} = 471\ MHz$ to $f_{res} = 492.5\ MHz$. However, the addition of the 0.2 mm substrate reduces the resonant frequency

to $f_{res} = 479\ MHz$ and the thicker substrate reduces it even further to $f_{res} = 439\ MHz$. This frequency is conveniently close to the desired operating frequency.

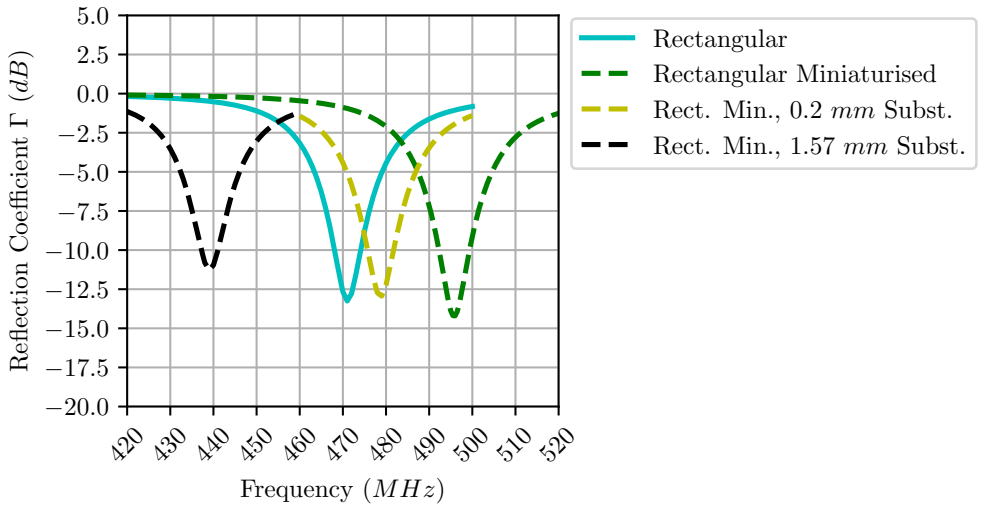

Figure 4.8: Reflection coefficient *Gamma* of the first rectangular FSRR configuration designed in section 4.3 versus the Γ of the antennas that fit the inner enclosure dimensions. The effect of adding substrate to the smaller model is also shown. The thicker substrate is used for manufacture.

The addition of the thicker substrate also significantly decreases the radiation efficiency of the first rectangular configuration model from $e_{rad} = 95.19\%$ to $e_{rad} = 80.81\%$. The thin substrate efficiency remains relatively high at $e_{rad} = 90.57\%$. The efficiencies and resonant frequencies for the configurations are summarised in Table 4.2.

The reduction in e_{rad} for the thicker substrate is substantial. However, the decrease in resonant frequency that it brings makes further tuning of the gap length viable. The same reduction in f_{res} could be achieved by using a lower loss substrate of similar ϵ_r, but this would increase costs. This type of substrate was not available for the project at the time of development, so the thicker FR-4 was used.

Table 4.2: The parameters of the rectangular FSRR antenna configuration compared to the miniaturised rectangular FSRR antenna and miniaturised rectangular FSRR antenna with different substrate thicknesses.

Parameters	**Rectanglular**	**Rectangular miniaturised**	**Rect. min.,** $0.2\ mm$ **subst**	**Rect. min.,** $1.57\ mm$ **subst**
$f_{res}\ (MHz)$	471	492.5	479	439
$e_{ref}\ (\%)$	95.27	95.61	94.92	92.54
$e_{rad}\ (\%)$	95.19	95.42	90.06	80.81
$e_{tot}\ (\%)$	90.69	91.23	85.971	74.78

4.5 Effect of the Inner Feed

The current configuration, which is shown to the left in Figure 4.9, has a large surface area of FR-4 in its centre. It was suggested that the sensor's electronics could be incorporated onto the antenna substrate to reduce the volume occupied in the enclosure. To allow this, the antenna's feed should face inward so that the electronics can be connected directly to it. This would require placing the feed on the inner conductor. This configuration was adapted from the thick substrate configuration in FEKO and is shown to the right in Figure 4.9 with a representation of the area required for the sensor electronics. It should be noted that the electronics were not included in the simulation.

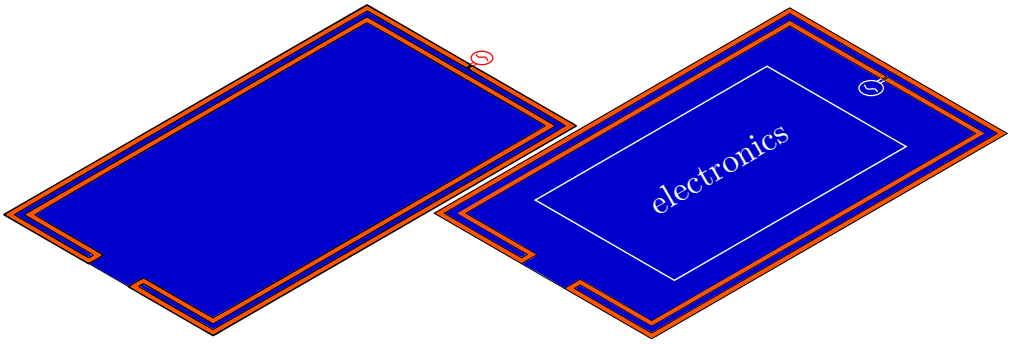

Figure 4.9: Model of the rectangular planar FSRR on the left, with an inward facing feed on the right. The configuration will allow sensor electronics to be incorporated onto the substrate.

The conductor width w_1 now refers to the inner coductor and w_2 to the

outer conductor. The directivity pattern was not expected to change because the shape of the antenna remains similar, and so only efficiencies were examined. The reflection coefficients for the inner-facing feed configuration and the miniaturised rectangular configuration are shown in Figure 4.10.

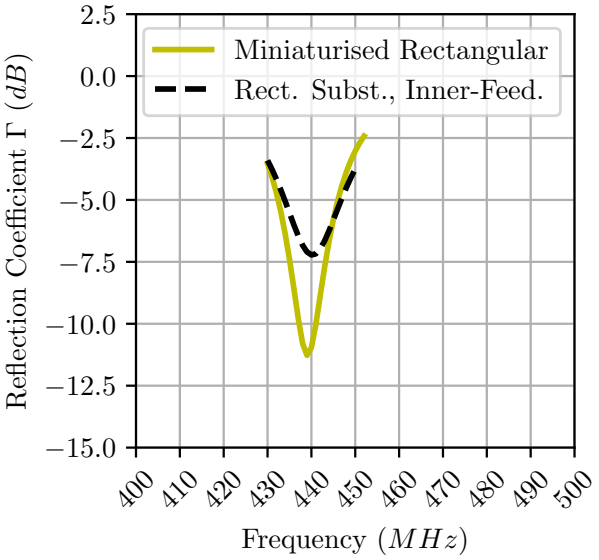

Figure 4.10: Reflection coefficient plot for the rectangular FSRR with its feed 'inverted' to face inside.

The reflection coefficient of the inner-facing feed model is increased from $\Gamma = -11.27\ dB$ to $\Gamma = -7.22\ db$ and is now above the required Γ value. This is a result of the input resistance being reduced from $R_{in} = 28.69\ \Omega$ to $R_{in} = 19.83\ \Omega$.

The efficiencies are given in Table 4.3. The main contributor to the decreased total efficiency of the inner feed model is the reflection efficiency of $e_{ref} = 81.04\%$. Similar to the first rectangular transformation described in Section 4.4, this transformation causes a decrease in R_{in}. Once again, it is assumed that the input resistance may be sufficiently raised by increasing the w_2/w_1 conductor ratio. Therefore, this model will be used for the proceeding designs. In future it is recommended that the effects of adding a ground plane to the centre of the antenna are evaluated, to approximate the incorporation of the sensor electronics.

Table 4.3: Parameters of the FSRR antenna with an outer and inner feed.

Parameters	**Rectangular substrate**	**Rect. subst. inner-feed**
f_{res} (MHz)	439	440
e_{ref} (%)	92.54	81.04
e_{rad} (%)	80.81	79.07
e_{tot} (%)	74.78	64.08

4.6 Tuning and Construction

This section describes the process of tuning the inner-facing feed model. The presence of the thick dielectric resulted in long solution times and made standard optimisation infeasible so the parameters were tuned manually.

The transformation from the inner-facing feed model described in Section 4.5 to a tuned model is shown in Figure 4.11 and the corresponding parameters in Table 4.4. The antenna length and breadth remain unchanged from the inner feed model throughout the tuning process. To increase the input resistance to be closer to 50 Ω, the conductor ratio was increased to $w_2/w_1 = 5.67$. This increased R_{in} from $R_{in} = 19.83\ \Omega$ to $R_{in} = 53.64\ \Omega$. To maintain the antenna length and breadth with an increased w_2/w_1 ratio the conductor's surface area was extended towards the antenna's centre. This decreases the electrical length because the current path is now shorter. So f_{res} increases from 440 MHz to 445 MHz.

Table 4.4: The dimensions of the inner feed FSRR antenna and its dimensions after it has been tuned.

Parameters	**Inner Feed Model**	**Tuned Model**
gl (mm)	10.40	6
s (mm)	3.13	2.66
w_1 (mm)	1.46	0.7
w_2 (mm)	1.46	4.08
w_2/w_1	1	5.67

The gap length was then decreased from 10.40 mm to 6 mm in order to lower f_{res}. Because the antenna length and breadth are fixed, decreas-

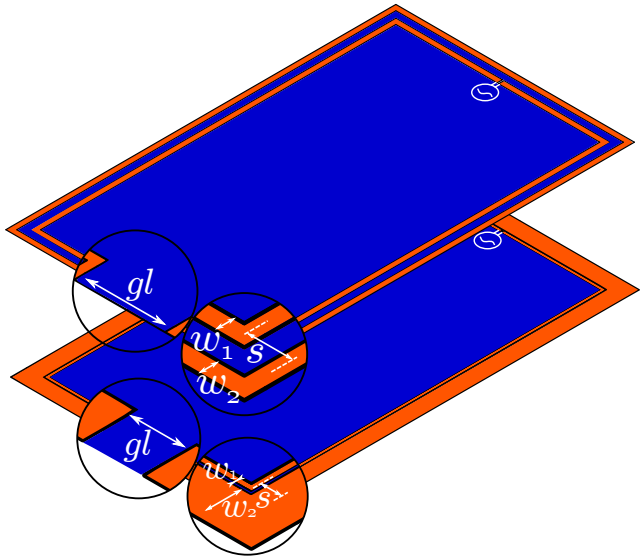

Figure 4.11: The upper inner feed model is tuned to produce the lower model. gl is decreased and w_2/w_1 is increased.

ing the gap extends the conductor length. So f_{res} decreases due to a combined electrical length extension and increased capacitance. It decreases from $f_{res} = 445\ MHz$ to $f_{res} = 429\ MHz$.

This resonant frequency was chosen at a lower value in anticipation that the constructed model would resonate at a slightly higher frequency than its simulated counterpart. The decision was prompted by the reflection coefficient measurement of an initial model similar to the tuned inner-facing model. The reflection coefficient and parameters of this model are given in Appendix A. The parameters of the inital tuned inner-feed model differed slightly to the current tuned inner-facing model, but it was machined using the same process and it also incorporated an ATB2012E balun. Therefore, it was believed that the discrepancies between measured and simulated values may be replicated for similar models. The simulated resonant frequency of the initial tuned inner-feed model was $f_{res} = 431.5\ MHz$ and the corresponding measured resonant frequency was $f_{res} = 434\ MHz$. This is a frequency difference of $2.5\ MHz$. The current inner-facing model should therefore have been chosen to resonate at $430.5\ MHz$. It was chosen to resonate at $429\ MHz$ because each simulation that was run required substantial time to complete and many simulations would have been required to tune the current inner-feed antenna to the exact resonant frequency of $429\ MHz$. Therefore, the resonant frequency

of $f_{res} = 429\ MHz$ was deemed to be satisfactory.

4.6.1 Construction

The tuned rectangular model was constructed using the same processes described in Chapter 3. The resulting model is shown in Figure 4.12(a), with the small ATB2012E-50011M SMT transformer balun attached. Once again a half-size scaled model was produced for pattern measurements. Ideally, the scaled substrate thickness would be 0.79 mm. Here, the closest available substrate thickness of 0.5 mm was chosen. The previous scaled model's substrate thickness was not scaled and its radiation pattern was accurate so the substrate thickness of 0.5 mm was deemed acceptable. A plastic ring is also no longer required to maintain the structure shape. The model is shown mounted in the anechoic chamber in Figure 4.12(b).

4.7 Measurement and Results

Measurements were carried out using the same equipment used in Section 3.5. However, it was opted to measure the gain in addition to the directivity for this antenna. This would allow the radiation efficiency to be determined by dividing the gain by the directivity, as shown in Equation 2.24.

The three-antenna method was used to measure the gain. This method involves measuring the received to transmitted power ratios for three different combinations of the reference antennas and AUT. The Friis transmission formula is then applied to each combination to solve for the individual antenna gain values [42]. The gain was measured toward $\theta = 0°$ and the RGP-10 horn and a log-periodic dipole array antennas were used as reference models.

The step-wise simulations that were performed throughout this chapter have shown the adaptation of the antenna's shape to fit the enclosure. We are now interested in validating the simulated tuned inner-fed miniaturised rectangular FSRR model from Section 4.6, by comparing it to the constructed equivalent. This model will henceforth be referred to as the 'adapted rectangular prototype'. Ideally, the performance of the adapted rectangular prototype

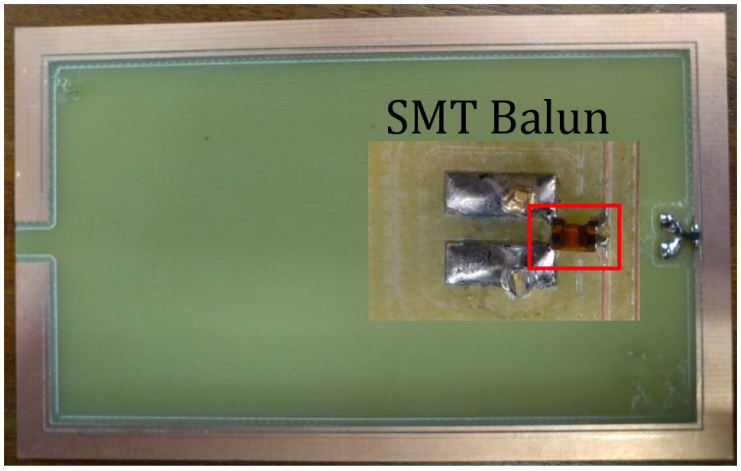

(a)

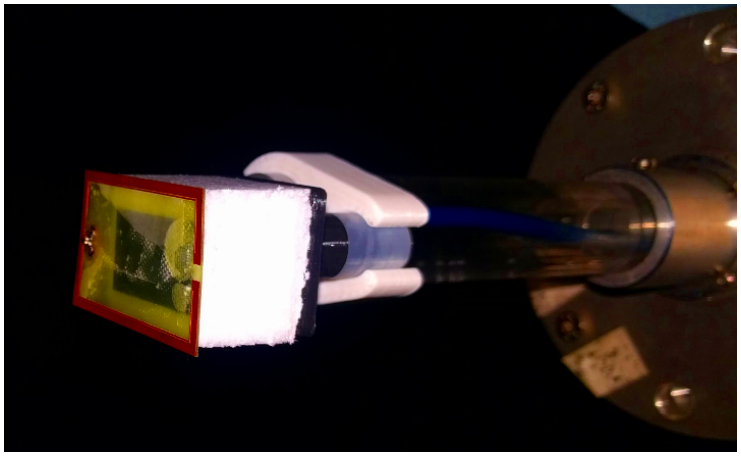

(b)

Figure 4.12: (a) The constructed rectangular FSRR antenna is shown, with a close-up of the SMT balun. The scaled model is shown inside the anechoic chamber in (b).

will at least be maintained compared to the circular prototype, which was designed in Chapter 3. Through the step-wise simulations it has been shown that this is generally not the case, however, and that trade-offs in performance will have to be made. These will be discussed in the final comparison between the constructed adapted rectangular prototype and the circular prototype.

The electrical size of the constructed adapted rectangular prototype antenna is $ka = 0.55$ which is larger than the circular prototype. For the project's purposes this is irrelevant because the antenna now fits inside the enclosure, but it didn't before.

4.7.1 Impedance

The reflection coefficient of the simulated and constructed adapted rectangular prototype antenna is shown in Figure 4.13. The simulated model's minimum reflection coefficient is $\Gamma = -33\ dB$ at $f_{res} = 429\ MHz$. The constructed model resonates 4 MHz higher at $f_{res} = 433\ MHz$, as predicted. At this frequency its reflection coefficient is $\Gamma = -19.77\ dB$ which results in a reflection efficiency of $e_{ref} = 98.95\%$. This is a slightly better match than the circular prototype from Chapter 3, whose reflection efficiency was $e_{ref} = 98.2\%$. The f_{res} deviation is small and predictable, so it does not pose a design problem. Hence, the impedance response of the simulated adapted rectangular prototype accurately represents the values measured for its constructed model and it performs better than the circular prototype.

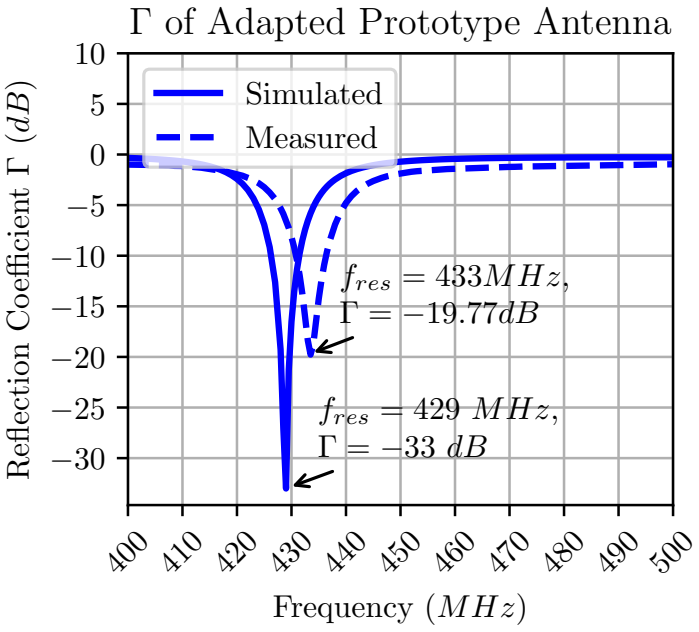

Figure 4.13: Reflection coefficients plotted for the simulated and constructed adapted rectangular prototype FSRR antenna.

4.7.2 Radiation

The directivity polar plots for the simulated and measured adapted rectangular prototype FSRR antennas at their resonant frequencies are shown in Figures 4.14(a), (b) and (c). The red solid trace indicates the directivity for the simulated adapted rectangular prototype in free-space. The maximum simulated directivity is 1.11 dBi for $\theta = 90°$, $\varphi = 0°$, as seen in Figure 4.14(a). This is only slightly lower than the circular prototype's maximum directivity of 1.26 dBi and is in the same direction. The minimum simulated directivity is -1.22 dBi, located in the $\varphi = 90°$ plane in Figure 4.14(b) toward $\theta = 90°$. This is an improvement of the minimum directivity compared to the circular prototype from Chapter 3, which was $D = -1.85$ dBi. This is consistent with Section 4.2 which found that the second rectangular configuration model (which the adapted rectangular prototype is based off of) had a more pronounced magnetic dipole mode than the planar circular model, and hence radiated more strongly in the direction of minimum radiation.

Thus, the adapted model successfully maintains its quasi-isotropic pattern.

The directivity of the measured adapted rectangular prototype is indicated by the dashed dark green trace in Figure 4.14(a), (b) and (c). It is suspected that the metal bracket is responsible for the creation of lobes towards the horizon, as in Section 3.5. In the $\varphi = 0°$ plane the maximum directivity is 3.63 dBi toward 76°. This is similar to the maximum measured directivity of the circular prototype which was $D = 3.99$ dBi, toward $\theta = 298$ °. The maximum directivity directions of both models are tilted upward, away from the horizon.

The influence of the metal bracket on the directivity plots is confirmed by including it in the simulation. The simulation is represented by the light blue dash-dotted trace in Figures 4.14(a), (b) and (c). The average directivity difference between measured and simulated models (taken over all directions) decreases when the bracket is added, from -4.39 dB without the bracket included in simulation to -8.85 dB with the bracket included in simulation. Therefore, similar to Section 3.5, the simulated adapted rectangular prototype should radiate similarly to an equivalent measured model without a bracket, with an average directivity error of approximately -8.85 dB . The model has thus been validated.

This is an improvement in measured directivity error compared to the circular prototype model. This is most likely a result of the higher accuracy with which the adapted rectangular prototype can be manufactured.

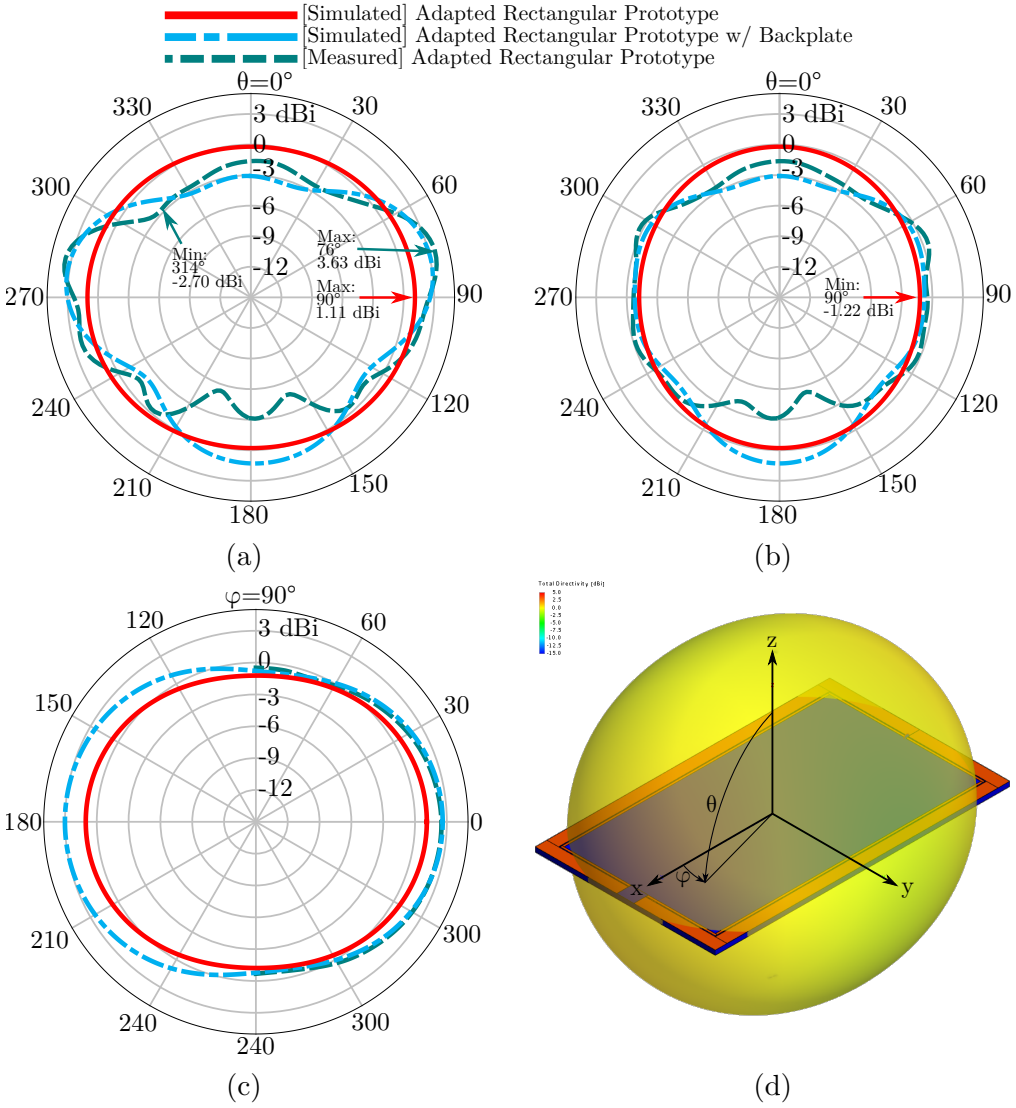

Figure 4.14: Far-field total directivity plots of the measured and simulated adapted rectangular prototype FSRR antenna. (a)-(c) The far-field polar plots of the measured and simulated antenna, simulations with and without a bracket, for (a) the $\varphi = 0°$ cut, (b) the $\varphi = 90°$ cut and (c) the $\theta = 90°$ cut. (d) The simulated 3-dimensional plot of the adapted rectangular prototype model without the bracket, whose orientation may be used as a reference for both simulated and measured models.

The measured radiation efficiency is $e_{rad} = 60.39\%$ at $f_{res} = 433\ MHz$, compared to the radiation efficiency of the simulated adapted prototype without a bracket of $e_{rad} = 76.86\%$. The difference is 15.82%, which is significant but consistent with the difference of 14.86% reported by Kim and Nam for their FSRR design, which was examined in Chapters 2 and 3 [39].

As mentioned in Section 4.4 the radiation efficiency may be raised by using a low loss substrate but, for this project, the option was not available. Furthermore, the tag will operate in an environment in which physical robustness will be an advantage. Given that the cost of a low loss substrate is substantially higher than the cost of FR-4, it could be argued that FR-4 would be preferred.

Aside from the discrepancy between simulated and measured radiation efficiency values, which is consistent with the literature, the simulated and measured traces align closely and so we can conclude that the simulated model has been validated.

4.7.3 Comparison

The measured values of the constructed circular prototype FSRR antenna and the constructed adapted rectangular prototype FSRR antenna are compared in Table 4.5. The ka of the adapted rectangular model is larger than the circular model because its corners expand further out from its centre. For this project's purposes, the antenna must fit inside the enclosure, so the larger ka of the adapted rectangular model is acceptable, as it comfortably fits inside. The low measured radiation efficiency e_{rad} pulls the total efficiency down to $e_{tot} = 60.39\%$ when multiplied by the reflection efficiency value $e_{ref} = 98.95\%$. The measured directivity values were used to calculate the realised gains in Table 4.5. These will be substituted for the simulated directivity values of both configurations, to remove the unwanted effects of the metal bracket on the radiation pattern. Therefore, the measured total directivity e_{tot} is multiplied by the simulated directivity to calculate the realised gain, in each case.

The maximum realised gain of the adapted prototype is now $G_{rl,max} = -1.03\ dBi$ and the minimum realised gain is $G_{rl,min} = -3.41\ dBi$. The max-

imum realised gain of the circular prototype is now $G_{rl,max} = 0.99\ dBi$ and the minimum realised gain is $G_{rl,min} = -2.12\ dBi$. The maximum and minimum realised gains of the adapted prototype fall below the required value of 0 dBi. If the radiation efficiency of the adapted prototype was increased to 79% or greater, its maximum realised gain would increase above the required minimum 0 dBi. If it was increased to $e_{rad} = 95.76\%$, which is the radiation efficiency of the circular prototype model, then the realised gain values of the adapted prototype would rise to $G_{rl,max} = 0.87\ dBi$ and $G_{rl,min} = -1.45\ dBi$. The minimum realised gain of the adapted prototype antenna would then be greater than the minimum realised gain of the circular prototype antenna. The maximum realised gain of the adapted prototype antenna would only be 0.12 dB lower than that of the circular prototype antenna. The adapted prototype could then be oriented to direct the maximum realised gain away from the ground and the project requirements would be satisfied. This could potentially be achieved by using a low loss substrate of a similar permittivity. Despite the extra expenses of such a substrate, its use is recommended to fully realise the potential of the adapted prototype FSRR antenna. Finally it should be highlighted that the adapted FSRR antenna outperforms the original bent monopole antenna, despite the reduced e_{rad}.

Table 4.5: The measured parameters of the circular prototype FSRR antenna from Section 3.5 and the adapted rectangular prototype FSRR antenna.

Params (mm)	**Circular Prototype, Measured**	**Adapted Prototype, Measured**
ka	0.48	0.55
e_{tot} (%)	94.04	60.39
$G_{rl,max}$ (dBi)	3.72	1.45
$G_{rl,min}$ (dBi)	-3.53	-4.98

4.8 Enclosure Measurements

In its operating environment, the FSRR antenna will be inside an enclosure with plastic walls and it will be in close proximity to the rhinoceros's body.

Both the rhinoceros's body and the enclosure's casing, which is made from a plastic called acetal, will act as dielectrics. As mentioned in Section 2.4 an antenna's resonant frequency and total efficiency (and hence the maximum realised gain) are reduced when brought in close proximity to a human body [16] [17]. A similar response is anticipated when the antenna is in close proximity to a rhinoceros's body. The enclosure's walls are much thinner than the body of an animal, so its effect on the antenna should be less pronounced.

Two experiments were conducted to establish the effect on the antenna's performance due to the presence of the enclosure and the rhinoceros's body. No radiation measurements were made due to time constraints and complications with scaling the enclosure with the antenna to operate above the anechoic chamber's lower frequency limit.

For the first experiment, the enclosure was modified to allow the reflection coefficient to be measured with the antenna inside. The antenna's position within the enclosure can be seen in Figure 4.15. It is $h_E = 24.43\ mm$ from the top of the enclosure. The enclosure wall thickness is $t_{EW} = 6\ mm$, its base thickness is $t_{EB} = 2\ mm$ and the lid thickness (which is not pictured) is 2 mm. The lid also has three 7 mm-wide support struts distributed along its width, which protrude inside the enclosure by 3 mm. The modified enclosure and antenna are pictured in Figure 4.16(a), and the measurement setup is shown in Figure 4.16(b).

For the following experiment, the antenna (still inside the enclosure) was

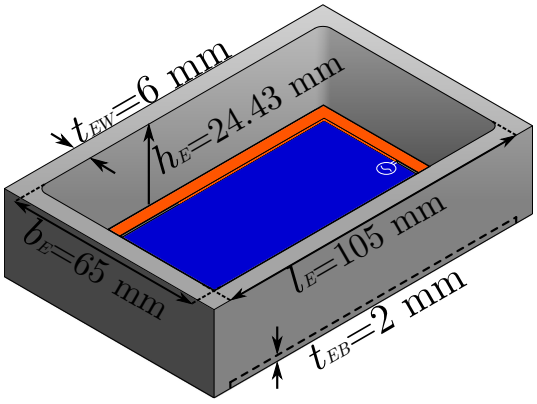

Figure 4.15: A representation of the adapted FSRR antenna placed inside of the enclosure.

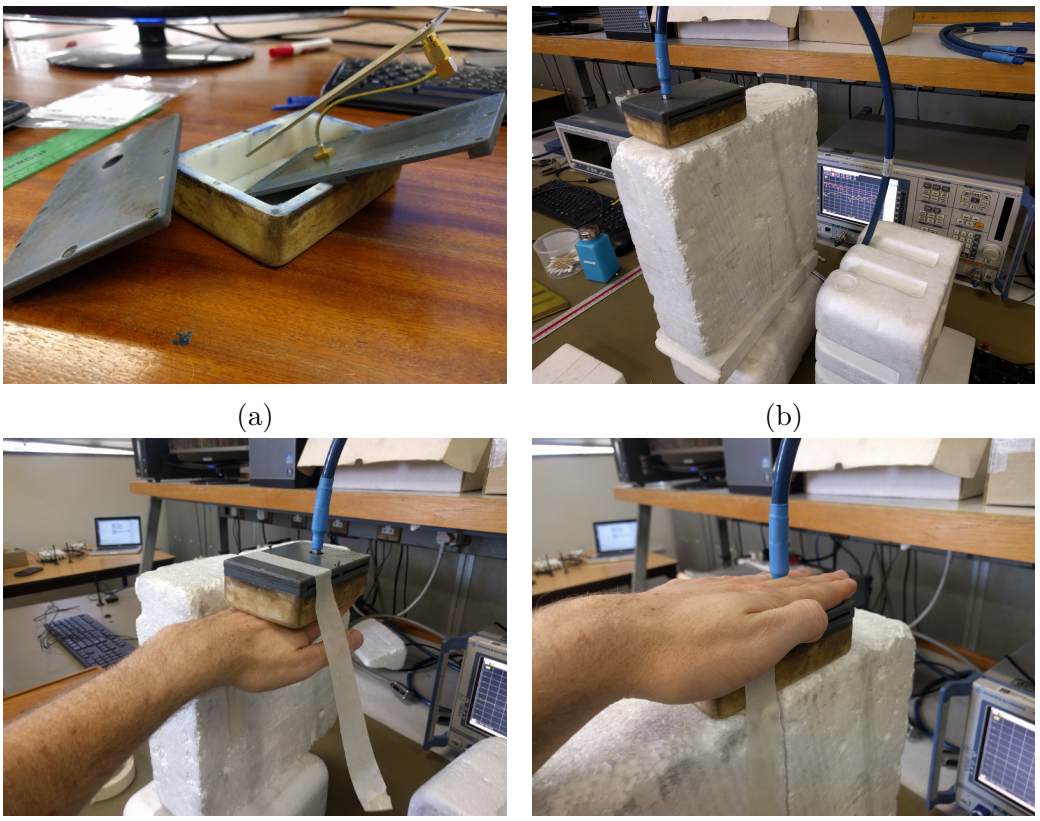

(a) (b)

(c) (d)

Figure 4.16: The modified enclosure is shown with the adapted FSRR antenna in (a). Measurement setups for the antenna inside the enclosure are shown for: (b) free-space, (c) toward and (d) away from a human hand.

brought in close proximity to a human hand, to approximate the combined effect that a rhinoceros's body would have on the antenna, together with the enclosure. The two variations of this second experiment are shown in Figures 4.16(c) and 4.16(d), with the antenna closer and further away from the hand, respectively. For the variation when the antenna is close to the hand, it is separated by 2 mm of plastic. When it is further from the hand, is is separated by 2 mm of plastic and 24.43 mm of air.

The reflection coefficient for the experiments is shown in Figure 4.17, with the enclosure experiment represented by the top figure and the hand proximity experiment represented by the bottom figure. The top figure is initially examined. By placing the antenna inside the enclosure, the antenna's resonant frequency moves from $f_{res=433.5\ MHz}$, represented by the blue trace, to

386 MHz, represented by the dashed green trace. This suggests that the antenna could be miniaturised by a factor of approximately 11% by applying the frequency scaling theorem.

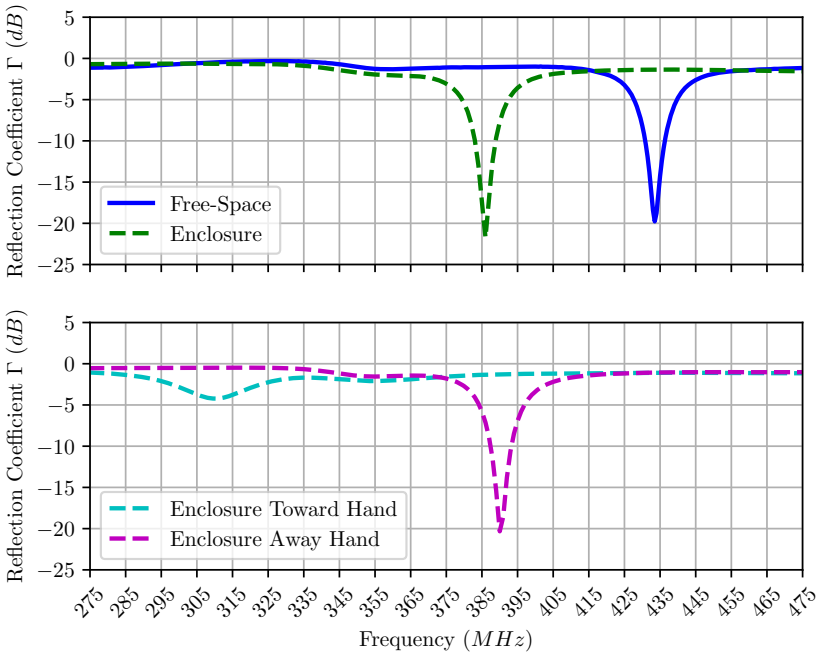

Figure 4.17: Reflection coefficient for the FSRR antenna, inside the enclosure and near a human hand. Top: In free space and inside the enclosure. Bottom: In close proximity to a human hand.

In the bottom figure the dashed cyan trace corresponds to figure 4.16(c), where the antenna is close to the hand. The effect is to further decrease the f_{res} to $f_{res} = 310\ MHz$. Furthermore, the input resistance R_{in} decreases to $R_{in} = 13.3\ \Omega$ at the resonant frequency, compared to the adapted prototype antenna in free-space with $R_{in} = 53.1\ \Omega$ at its resonant frequency. This indicates that the arm lowers the radiated power, most likely due to absorption.

The reversed enclosure reflection coefficient, where the antenna is further away from the arm as in Figure 4.16(d), is given by the dashed magenta trace. The f_{res} increases to $f_{res} = 390\ MHz$ and the R_{in} increases to $R_{in} = 42.2\Omega$.

These findings are generally consistent with work carried out by Tuovinen et. al [16] [17]. It is suggested that the antenna be placed as far away from the

rhinoceros tissue as possible to prevent negative effects to the impedance. The enclosure should be orientated accordingly. It is also recommended that the antenna size be decreased by approximately 11% to increase f_{res} to 433.5 Mhz. However, this value could change depending on where the antenna is placed inside the enclosure.

Further investigations could examine the effect on the radiation pattern. This should be done in an anechoic chamber that operates at the required frequency so that the original sized enclosure can be used.

4.9 Summary and Conclusion

The circular prototype FSRR antenna from Chapter 3 was adapted to fit inside of the animal borne enclosure. It was first transformed from a 3-dimensional to a planar form, in order to allow the incorporation of a small SMT balun. This model was then transformed into two variations of a rectangular shape, to coincide with the shape of the enclosure. It was found that both variations raised the resonant frequency. The input resistance of the first rectangular configuration decreased, while the minimum directivity of the second rectangular configuration decreased. It was decided that the first configuration was the most promising design given that the input resistance could be raised by adjusting the tuning parameters. The first rectangular configuration was then miniaturised to fit comfortably inside of the enclosure and a 1.57 mm thick rigid substrate was added, which the antenna would be manufactured onto. The substrate decreased the resonant frequency and the radiation efficiency. The feed of the smaller rectangular model was then inverted to face inwards, so that sensor electronics could potentially be incorporated onto the centre of the substrate. This also lowered the input resistance. The tuning parameters of the inner facing feed model were then adjusted to achieve a good match and hence a high reflection efficiency. The resulting model, now referred to as the adapted prototype, was subsequently constructed and compared to its simulated counterpart. Good agreement was found between the two models. It was also compared to the circular prototype antenna from Chapter 3. The circular prototype antenna operated with higher radiation efficiency and hence

higher realised gain. However, it could not operate in the animal borne enclosure due to its size. It was recommended to use a low loss substrate of similar permittivity to increase the radiation efficiency. This would increase the cost of the model Finally, the reflection coefficient of the adapted prototype model was measured while the model was placed inside the enclosure, and in close proximity to a human arm. It was found that the antenna should be placed as far away from the human arm as possible to avoid an increase in mismatch.

Chapter 5

Conclusions and Recommendations

5.1 Project Overview

An electrically small antenna for use in an animal-borne behavioural monitoring system was designed and constructed. The base model was selected from a list of potential candidate antennas, based on specific design requirements. These requirements were formulated as part of the project. Primarily, the antenna had to radiate omnidirectionally with high radiation and reflection efficiencies at an electrically small size of $ka \leq 0.57$ at 433 MHz, in order to fit inside the enclosure.

The folded split ring resonator antenna was found to be the ideal candidate due to its small electrical size, high radiation and reflection efficiency, quasi-isotropic radiation pattern and its availability of tuning parameters. It also outperformed the original bent monopole antenna.

A model was then simulated to gain an understanding of the FSRR antenna's operating principles and to assess the effectiveness of the tuning parameters. It was found that small decreases to the resonant frequency could be made by decreasing the gap length. It was also found that increasing the conductor width ratio could dramatically increase the input resistance.

The simulated model was then optimised and constructed. The constructed

model was compared to the literature and was found to satisfy the design parameters, even though it was manufactured on more affordable, lossy FR-4 substrate. Despite this, the circular shape of the prototype, as well as the large sleeve balun that was attached to its terminals, prevented it from fitting inside of the rectangular enclosure.

To address this the circular antenna was then systematically adapted to the enclosure's shape. It was also reduced to a more rigid planar form to allow the mounting of a small surface mount balun. This change also made the manufacturing process easier. It was then transformed to a rectangular shape and miniaturised to fit inside the enclosure. Finally, it was modified to allow it to be fed from electronics located within the antenna on the same substrate. The gap length was decreased and the conductor ratio increased to achieve a high reflection efficiency.

This adapted antenna was then constructed, validated and compared to the previous circular model. It was found that the reflection efficiency of the adapted rectangular model was slightly higher than the circular model. The quasi-isotropic radiation pattern was also maintained. Unfortunately, the thicker FR-4 substrate used to provide the rectangular configuration's rigidity also decreased the radiation efficiency. This resulted in maximum and minimum realised gain values that did not satisfy the project requirements, despite being higher than the original bent monopole's realised gain values. It is recommended to alleviate this issue by replacing the FR-4 with a low loss dielectric of similar permittivity, such as Kappa 438 laminate from Rogers Corp. The substrate is more expensive, but it will enable the adapted prototype FSRR antenna to satisfy all of the design requirements.

Finally, tests were performed to assess the change in the adapted prototype antenna's reflection coefficient when it was placed inside the animal borne enclosure, and in close proximity to a human arm. It was found that placing the antenna inside the enclosure reduced its resonant frequency. According to the frequency scaling theorem, this indicates that the antenna structure may be further scaled down in size to raise the resonant frequency. When the antenna was brought in close proximity to the arm the resonant frequency and

the input resistance decreased further. This led to much greater mismatch. By reversing the enclosure so that the antenna faced further away from the arm the effects were drastically reduced. Therefore, the antenna should be placed as far away from the animal's body as possible.

5.2 Recommendations and Future Work

The work presented in this thesis can be extended in several ways, as described in the following.

1. The low radiation efficiency of the antenna should be improved by incorporating a low loss dielectric of comparable permittivity. A model incorporating this dielectric should be designed, constructed and tested for use in the animal borne enclosure.

2. The success of the inner facing feed acts as a first step towards incorporating the sensor electronics onto the enclosure. It is suggested that a ground plane is added to the antenna's centre, soldered to the balun return conductor and tested, in order to approximate the presence of electronics. This would allow the feasibility of incorporating the electronics to be tested. Ideally, they would have little effect on the antenna's performance.

3. Further research should be done on the effect of the enclosure on the antenna's performance, as well as the presence of rhinoceros tissue within the antenna's near-field. The research could be extended by measuring the response of the antenna's radiation pattern to these scenarios. An approximation of rhinoceros tissue has also been developed in a concurrent project by Mr. Van Zyl [5]. It is recommended to test the antenna's performance in close proximity to this tissue.

4. The lower frequency limit of the anechoic chamber in Stellenbosch University presents an obstacle to measuring the antenna's radiation patterns at the 433 MHz operating frequency. In this project, the scaling theorem was applied to construct half-sized models that operated above the chamber's lower limit. This added a lot of time to the design process.

Contact should be made with an external facility that offers anechoic chamber measurements at the required frequency to avoid this delay.

5. A plastic bracket should be designed to replace the metallic bracket that is used to mount the antenna inside the anechoic chamber. This should reduce the scattering effects which distort the measured radiation patterns.

Appendices

Appendix A

Additional Antennas

A.1 The Initial Tuned Inner-Feed Model

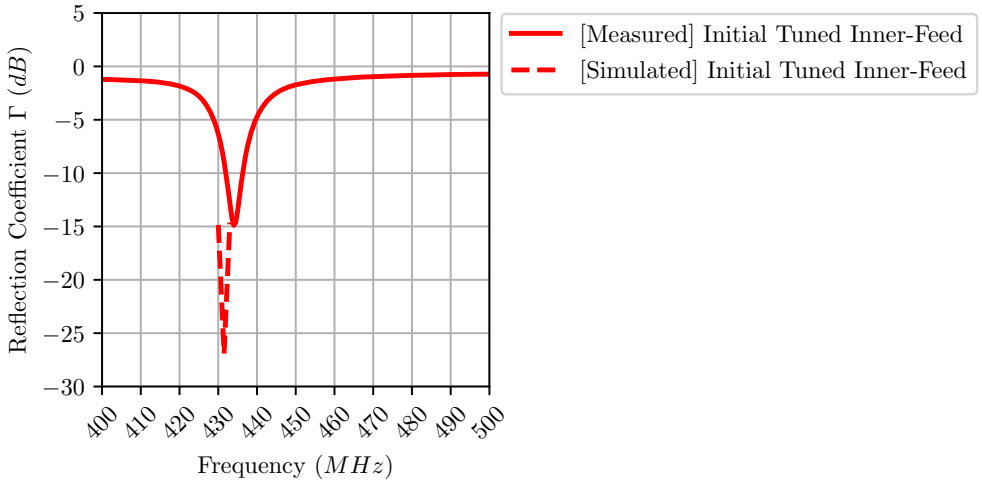

Figure A.1: Reflection coefficient of the initial inner feed model.

Table A.1: The dimensions of the initial inner-feed tuned FSRR antenna.

Parameters (mm)	**Init. Inner Feed Model**
gl	9.5
s	2.66
w_1	0.29
w_2	2.63
w_2/w_1	9.07

Appendix B

Datasheets

B.1 SL3101 Passive Iridium Antenna

B.2 ATB2012E Balun

Specifications

	Minimum	Typical	Maximum	Unit
Part Number	SL3101 (see page 8 for detailed part numbers)			Each
Type	Octafilar Helix			
Embedded Frequency	1616	1621	1626	MHz
Polarization	Right-hand circular polarized			
Gain		+2.0		dBic @ zenith
Efficiency		65%		Total spherical
Beamwidth		>120		Degrees
Bandwidth (1dB)		15		MHz
Axial Ratio		<1.5		@Zenith
VSWR		<2.0:1	2.3:1	
Impedance		50		
Operating Temperature	-40	+20	+85	°C
Element Dimensions	14 (diameter) x 33 (length)			mm
Overall Dimensions (radome)	19 (dia) x Connector dependent (length)			mm
Weight (including radome)	29, 48, 48 (SP, TJ, TP)			grams

(a)

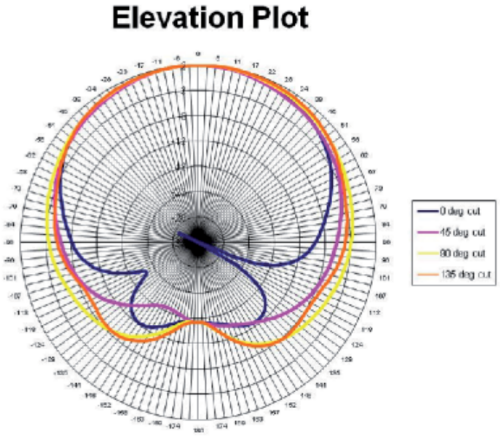

(b)

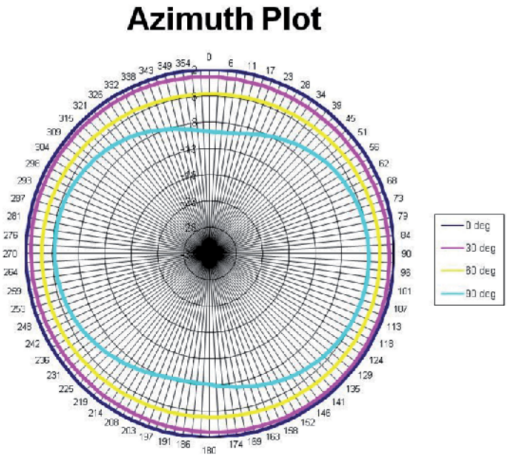

(c)

Figure B.1: In (a) the specifications of the passive iridium (octafilar helix) antenna. In (b) and (c) the total gain polar plots in the elevation and azimuth plane respectively. SOURCE: *SL3101 Passive Iridium Antenna Product Specification*, v4, Sarantel, Sep. 2009.

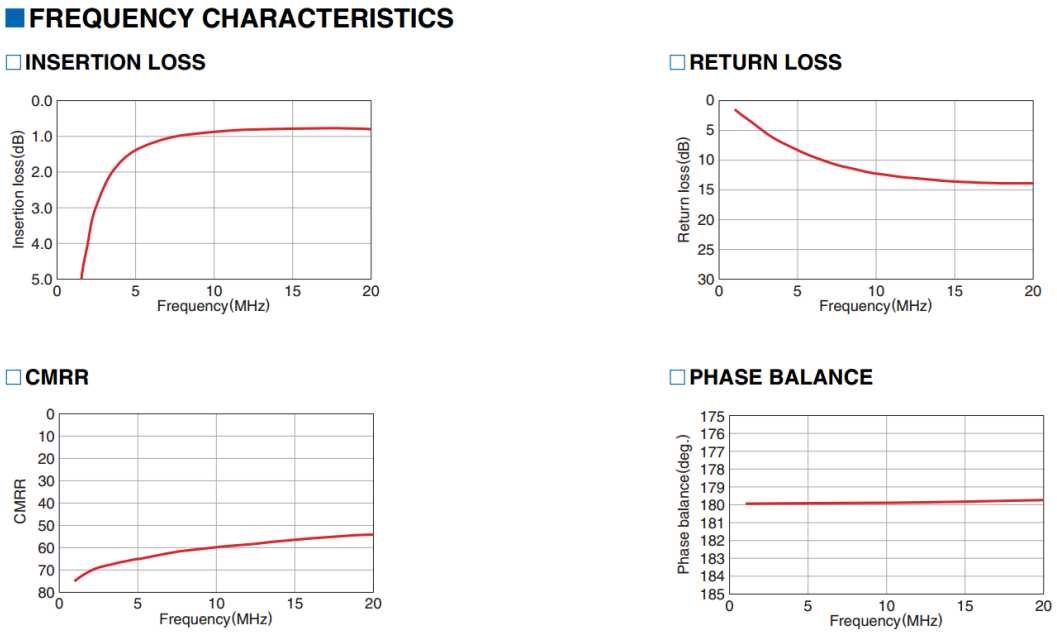

Figure B.2: Frequency characteristics of the ATB2012E balun. SOURCE: *ATB Series, Balun Transformers Datasheet*, TDK, Sep. 2017.

Appendix C

Python Code

C.1 Extract resonant frequencies from FEKO model sweep

```
import Fres_Func as swp
import numpy as np
import matplotlib.pyplot as plt
import os
import glob

def get_res_point(path, stdconfig_ref):
""" Populate a list of resonant points for a set of antenna configurations.
Files must be in the same order if using as alternate axis from get_cap_fname
"""
res = []
stdconfig = []
res_temp = []
#Values
freq = 0
s11 = 0

#Keys
freq_key = 'FREQ =    '
s11_key = 'S     1      1'
```

```
stdconfig_key = 'StandardConfiguration'

#Positions
freq_pos = 5
s11_pos = 6
stdconfig_pos = 21

for filename in glob.glob(os.path.join(path, '*.out')):
file_handler = open(filename, 'r')
for line in file_handler:
if stdconfig_key in line:
stdconfig = line.split()
stdconfig = float(stdconfig[1][stdconfig_pos])
if freq_key in line and stdconfig == stdconfig_ref:
freq = float(line.split()[freq_pos])
if s11_key in line and freq != 0 and stdconfig == stdconfig_ref:
s11 = float(line.split()[s11_pos])
tup_temp = (freq, s11)
res_temp.append(tup_temp)
freq = 0
res_temp_sort = sorted(res_temp, key = lambda restemp: restemp[1])
#Extract the minimum S11
res.append(res_temp_sort[0][0])
del res_temp[:]
del res_temp_sort[:]
return res

def sortcomb_xy(x, y):
"""
Combine XY coordinates into a single list.
Order list in ascending order.
"""
xy = []

temp = zip(x, y)
```

```
temp.sort()
xy = zip(*temp)

return xy

Path = r'C:\Sam Masters\Simulations\Chapter
 4\Split Length Sweep\PEC Model\1 MHz Res'

c0 = 299792458.000176
Reference_Freq = 433E6
wavelength_mm = (c0/Reference_Freq)*1000

columnwidth = 5.515748
pageheight = 8.9448819

title_name1 = '$f_{res}$ of FSRR antenna for varying $gl$.'

yname ='Resonant Frequency $f_{res}$ $(MHz)$'
xname = 'Gap Length $gl$ ($\lambda$)'

gl_min = 1
gl_max = 25
gl_step=0.5

tickfontsize = 10
xlabelfontsize = 10
ylabelfontsize = 10
titlefontsize = 12

#Original Optimized Antenna
Resonant = []
Capacitance = []
ScaleFactor = []
EFF = []
Resonant_xy = []
```

```
ScaleFactor_xy = []
Radres = []
Radres_SF = []
EFF_SF = []

#Get Capacitance, Resonance and other Values.
Resonant_Hz = swp.get_res_point(Path, 2)
Resonant_MHz = []
#Convert to MHz
epsilon = 10**(-6)
for res in Resonant_Hz:
Resonant_MHz.append(res*epsilon)

gl = np.arange(gl_min, gl_max + gl_step, gl_step)
gl_lamb = gl/wavelength_mm

ymin = 410
ymax = 440
ystep = 3

xmin = 0
xmax = max(gl_lamb)
xstep = (0.004)

#Combine and Order XY Values
Resonant_xy = swp.sortcomb_xy(gl_lamb, Resonant_MHz)

plt.rc('text', usetex=True)
plt.rc('font', family='serif', serif = ['Computer Modern'])
ax = []

fig = plt.figure()
fig.set_size_inches((columnwidth*0.48), (pageheight/3.5))

# Create a list of axes.
```

```
ax1 = fig.add_subplot(1, 1, 1)

#Plot Capacitance with Resonant Points
ax1.plot(Resonant_xy[0], Resonant_xy[1],
 color = 'darkmagenta', linewidth = 2)

ax1.grid(True, which = 'major', linestyle = '-')

ax1.set_xlabel(xname, fontsize = xlabelfontsize)
ax1.set_ylabel(yname, fontsize = ylabelfontsize)
#ax1.set_title(title_name1, fontsize = 12)

ax1.set_xlim(xmin, xmax)
ax1.ticklabel_format(style = 'sci',axis='x', scilimits=(0,0))
ax1.set_xticks(np.arange(xmin, xmax + xstep, xstep))
#ax1.set_yticks(np.arange(ymin, ymax + ystep, ystep))

ax1.annotate('Orig. Antenna \n $0.019\~\lambda$, \n $433.67\~MHz$',
xy=(0.02, 433.668),  # theta, radius
            xytext=(-25, -40),    # fraction, fraction
            textcoords='offset points',
arrowprops=dict(arrowstyle="->"))

for tick in ax1.get_xticklabels():
tick.set_rotation(45)

plt.show()

fig.savefig('fres_glsweep.pdf', bbox_inches = 'tight')
```

C.2 Plot single image with outer legend

```
import numpy as np
import pandas as pd
import os
```

```
import glob
import matplotlib.pyplot as plt

columnwidth = 5.515748
pageheight = 8.9448819

path = r'C:\Users\16522370\Documents\Sam Masters\Thesis\
masters-repo\Python\Chap-5'
filename1='reflcoeff_recttransform.dat'
measline1 = 444
measline2 = 478
#Plotting Parameters

yname1 ='Reflection Coefficient $\Gamma$ $(dB)$'
xname = 'Frequency $(MHz)$'

tickfontsize = 10
xlabelfontsize = 10
ylabelfontsize = 10
titlefontsize = 12

df1 = pd.read_csv(filename1,
header = 0,
index_col = 0,
delim_whitespace = True
) #

style1 = ['m', 'c--', 'g--' ]
#Convert to MHz
epsilon = 10**(-6)
df1.index = (df1.index*epsilon)

xmin = 400
xmax = 500
xstep = 10
```

```
ymin1 = -45
ymax1 = 5
ystep1 = 5

plt.rc('text', usetex=True)
plt.rc('font', family='serif',
serif = ['Computer Roman Modern']
)

fig = plt.figure()
fig.set_size_inches((columnwidth), (3))
ax1 = fig.add_subplot(1, 2, 1)

plt.legend(loc = 'upper left', frameon = 'False')

df1.plot (style = style1,
linewidth = 2,
fontsize = tickfontsize,
ax = ax1
)
ax1.plot([measline1, measline1],
[ymin1,ymax1],
linewidth = 1.5,
color = 'black',
linestyle = '--'
)
ax1.plot([measline2, measline2],
[ymin1,ymax1],
linewidth = 1.5,
color = 'black',
linestyle = '--'
)
#ax2 = ax.twinx() # Allows for a secondary axis to be plotted
```

```
ax1.annotate('$444\ MHz$',
xy=(444, ymin1),  # theta, radius
xytext=(3, 3),    # fraction, fraction
textcoords='offset points',
arrowprops=dict(arrowstyle="-"))

ax1.annotate('$478\ MHz$',
xy=(478, ymin1),  # theta, radius
xytext=(3, 3),    # fraction, fraction
textcoords='offset points',
arrowprops=dict(arrowstyle="-"))


plt.suptitle(title_name1, fontsize = 12)

# Shrink current axis by 20%
box = ax1.get_position()
ax1.set_position([box.x0, box.y0,
box.width * 0.8, box.height
])

# Put a legend to the right of the current axis
ax1.legend(loc='center left',
bbox_to_anchor=(1, 0.85)
)

ax1.grid(True, which = 'major', linestyle = '-')

ax1.set_xlabel(xname,
fontsize = xlabelfontsize
)
ax1.set_ylabel(yname1,
fontsize = ylabelfontsize
)
```

```
ax1.set_xlim(xmin, xmax)
ax1.set_ylim(ymin1, ymax1)
ax1.set_xticks(np.arange(xmin, xmax + xstep, xstep))
ax1.set_yticks(np.arange(ymin1, ymax1 + ystep1, ystep1))

for tick in ax1.get_xticklabels():
tick.set_rotation(45)

plt.tight_layout()
fig.savefig("reflcoeff_recttransform.pdf", bbox_inches='tight')
plt.show()
```

Bibliography

[1] R. Emslie et al., "African and asian rhinoceroses - status, conservation and trade", IUCN Species Survival Commission, Gland, Switzerland, Vaud, 17.

[2] S. Le Roux, "A prototype animal borne behaviour monitoring system", M.S. thesis, Stellenbosch Univ., Stellenbosch, 2016.

[3] S. le Roux et al., "Energy benefits of on-board behaviour classification for animal-borne sensor applications", in *Proc. 2017 IEEE Robotics Conf.*, Glasgow, Scotland, UK, 2017, pp. 1–3.

[4] M. Struwig et al., "Non-linear model and method of optimization for a single-axis linear-motion energy harvester", *unpublished*,

[5] F. J. van Zyl, "Characterisation of the dielectric properties of rhinoceros tissue using computer simulation and physical tissue phantom models", M.S. thesis, Stellenbosch Univ., 2017.

[6] J. Wotherspoon, "Choosing an integreated RF module", in *AFRICON, 2017*, 2017, pp. 1–6.

[7] P.-S. Kildal, *Foundations of Antenna Engineering: A Unified Approach for Line-Of-Sight and Multipath*, 1st. Kildal, Oct. 14, 2015, p. 33.

[8] C. A. Balanis, *Antenna Theory: Analysis and Design*, 3rd. Hoboken, NJ: Wiley-Interscience, 2005, p. 1039.

[9] J. L. Volakis, *Antenna engineering handbookThomas F. Eibert*, 4th ed., ser. McGraw-Hill's AccessEngineering. New York: McGraw-Hill, 2007, vol. 1, 1753 pp.

[10] C. A. Balanis, *Antenna Theory: Analysis and Design*, 3rd. Hoboken, NJ: Wiley-Interscience, 2005, p. 71.

[11] J. S. Seybold, *Introduction to RF Propagation*. Hoboken, NJ: Wiley-Interscience, 2005, 330 pp.

[12] P.-S. Kildal, *Foundations of Antenna Engineering: A Unified Approach for Line-Of-Sight and Multipath*, 1st. Kildal, Oct. 14, 2015, p. 65.

[13] C. A. Balanis, *Antenna Theory: Analysis and Design*, 3rd. Hoboken, NJ: Wiley-Interscience, 2005, p. 34.

[14] J. S. McLean, "A re-examination of the fundamental limits on the radiation q of electrically small antennas", *IEEE Transactions on antennas and propagation*, vol. 44, no. 5, p. 672, 1996.

[15] H. A. Wheeler, "The radiansphere around a small antenna", *Proceedings of the IRE*, vol. 47, no. 8, pp. 1325–1331, Aug. 1959.

[16] T. Tuovinen et al., "Reactive near-field region radiation of planar UWB antennas close to a dispersive tissue model", in *Antennas and Propagation Conference (LAPC), 2012 Loughborough*, IEEE, 2012, pp. 1–4.

[17] T. Tuovinen et al., "Effect of the antenna-human body distance on the antenna matching in UWB WBAN applications", in *2013 7th International Symposium on Medical Information and Communication Technology (ISMICT)*, Mar. 2013, pp. 193–197.

[18] R. F. Harrington, "Effect of antenna size on gain, bandwidth, and efficiency", *J. Res. Nat. Bur. Stand*, vol. 64, no. 1, pp. 1–12, 1960.

[19] L. J. Chu, "Physical limitations of omni-directional antennas", *Journal of Applied Physics*, vol. 19, no. 12, p. 1163, 1948.

[20] P.-S. Kildal, *Foundations of Antenna Engineering: A Unified Approach for Line-Of-Sight and Multipath*, 1st. Kildal, Oct. 14, 2015, p. 136.

[21] C. A. Balanis, *Antenna Theory: Analysis and Design*, 3rd. Hoboken, NJ: Wiley-Interscience, 2005, pp. 513–517.

[22] R. Lampe, "Design formulas for an asymmetric coplanar strip folded dipole", *IEEE transactions on antennas and propagation*, vol. 33, no. 9, pp. 1028–1031, 1985.

[23] K. Fujimoto and H. Morishita. Cambridge, 2014, p. 52.

[24] J. L. Volakis, *Antenna engineering handbookThomas F. Eibert*, 4th ed., ser. McGraw-Hill's AccessEngineering. New York: McGraw-Hill, 2007, vol. 1, p. 139.

[25] W. W. Cochran and R. D. Lord, "A radio-tracking system for wild animals", *The Journal of Wildlife Management*, vol. 27, no. 1, p. 9, Jan. 1963.

[26] G. Garshelis and B. Donald, "Evaluation of radio-transmitter attachments for sea otters", *Wiley, Wildlife Society*, vol. 11, no. 4, pp. 378–383, 1983.

[27] M. Green et al., "Radio-telemetry observations of the first 650 km of the migration of bar-tailed godwits limosa lapponica from the wadden sea to the russian arctic", *Ardea*, vol. 90, no. 1, pp. 71–80, 2002.

[28] J. M. Martin et al., "Methodology for efficiency measurements of electrically small monopoles for animal tracking", *Antennas and Propagation Magazine, IEEE*, vol. 51, no. 2, pp. 39–47, 2009.

[29] R. MacCurdy et al., "Automatic animal tracking using matched filters and time difference of arrival.", *JCM*, vol. 4, no. 7, pp. 487–495, 2009.

[30] W. Bouten et al., "A flexible GPS tracking system for studying bird behaviour at multiple scales", *Journal of Ornithology*, vol. 154, no. 2, pp. 571–580, Apr. 2013.

[31] C. A. Balanis, *Antenna Theory: Analysis and Design*, 3rd. Hoboken, NJ: Wiley-Interscience, 2005, p. 232.

[32] J. L. Volakis, *Antenna engineering handbookThomas F. Eibert*, 4th ed., ser. McGraw-Hill's AccessEngineering. New York: McGraw-Hill, 2007, vol. 1, p. 141.

[33] *SL3101 Passive Iridium Antenna Product Specification*, Sarantel, Sep. 2006.

[34] O. Leisten, "Capability and Manufacturability: Some Considerations Concerning the Current Status of Multi-Filar Dielectric Loaded Antennas", presented at the Antennas and Propagation Conference (LAPC), 2014 Loughborough, Loughbrorough, UK: IEEE, Oct. 2014, pp. 7–12.

[35] C. Rowell and E. Y. Lam, "Mobile-phone antenna design", *IEEE Antennas and Propagation Magazine*, vol. 54, no. 4, pp. 14–34, 2012.

[36] M. Ali and G. J. Hayes, "Analysis of integrated inverted-F antennas for Bluetooth applications", in *Antennas and Propagation for Wireless Communications, 2000 IEEE-APS Conference On*, IEEE, 2000, pp. 21–24.

[37] J. B. Pendry et al., "Magnetism from Conductors and Enhanced Nonlinear Phenomena", *IEEE transactions on microwave theory and techniques*, vol. 47, no. 11, pp. 2075–2084, 1999.

[38] Yuandan Dong and T. Itoh, "Metamaterial-Based Antennas", *Proceedings of the IEEE*, vol. 100, no. 7, pp. 2271–2285, Jul. 2012.

[39] J.-H. Kim and S. Nam, "A Compact Quasi-Isotropic Antenna Based on Folded Split-Ring Resonators", *IEEE Antennas and Wireless Propagation Letters*, vol. 16, pp. 294–297, 2017.

[40] C. A. Balanis, *Antenna Theory: Analysis and Design*, 3rd. Hoboken, NJ: Wiley-Interscience, 2005, p. 539.

[41] S. A. Saario et al., "Full-wave analysis of choking characteristics of sleeve balun on coaxial cables", *Electronics letters*, vol. 38, no. 7, pp. 304–305, 2002.

[42] C. A. Balanis, *Antenna Theory: Analysis and Design*, 3rd. Hoboken, NJ: Wiley-Interscience, 2005, p. 1031.